

Journal of Materials Chemistry A

Materials for energy and sustainability

Accepted Manuscript

This article can be cited before page numbers have been issued, to do this please use: X. Mao, M. Sarkar and J. He, *J. Mater. Chem. A*, 2026, DOI: 10.1039/D5TA09312K.



This is an Accepted Manuscript, which has been through the Royal Society of Chemistry peer review process and has been accepted for publication.

Accepted Manuscripts are published online shortly after acceptance, before technical editing, formatting and proof reading. Using this free service, authors can make their results available to the community, in citable form, before we publish the edited article. We will replace this Accepted Manuscript with the edited and formatted Advance Article as soon as it is available.

You can find more information about Accepted Manuscripts in the [Information for Authors](#).

Please note that technical editing may introduce minor changes to the text and/or graphics, which may alter content. The journal's standard [Terms & Conditions](#) and the [Ethical guidelines](#) still apply. In no event shall the Royal Society of Chemistry be held responsible for any errors or omissions in this Accepted Manuscript or any consequences arising from the use of any information it contains.

Design of Polymer–Metal Nanocatalyst Interfaces for Electrochemical CO₂ Reduction Reactions

Xi Mao,^a Manthan Sarkar,^b Jie He*^{ab}

^a Polymer Program, Institute of Materials Science, University of Connecticut, Storrs, Connecticut 06269, USA

^b Department of Chemistry, University of Connecticut, Storrs, Connecticut 06269, USA

* Email: jie.he@uconn.edu

ABSTRACT

Electrochemical CO₂ reduction reactions (eCO₂RRs) offer a promising strategy for carbon cycling by converting the greenhouse gas CO₂ into value-added chemicals or fuels. Metal nanocatalysts are among the most desirable catalysts for facilitating CO₂ activation. However, achieving high activity, selectivity, and long-term stability in these nanocatalysts remains challenging. Surface modification with synthetic polymer ligands offers an alternative route to resolve those challenges in eCO₂RR without redesigning nanocatalysts themselves. Most recent studies suggest that polymers not only enhance the structural stability of metal nanocatalysts but also provide an interfacial microenvironment that improves eCO₂RR through multiple mechanisms, including increasing local CO₂ concentration, stabilizing intermediates, and suppressing competitive proton reduction. In this review, we summarize the recent advances in eCO₂RRs using metal nanocatalysts modified with polymer ligands, including nanocatalysts with hydrophobic, conductive, ionic and porous polymers. We discuss the mechanistic insights underlying polymer-catalyst interactions, with particular emphasis on how these interactions enhance catalytic performance. Finally, we conclude with key challenges and highlight future perspectives in this field.

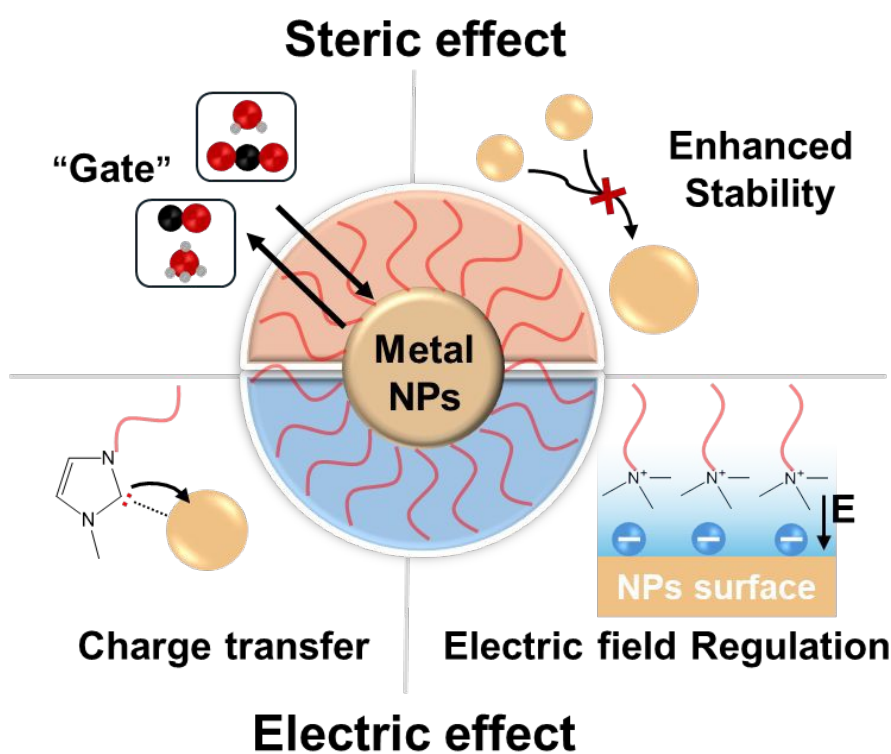
1. Role of surface ligands in catalysis

Metal nanoparticles (NPs) play a central role in heterogeneous catalysis.¹ Due to their ultrasmall dimensions, metal NPs exhibit distinct “nano effects” (or a high surface-to-volume ratio) that significantly enhance catalytic reactivity relative to their bulk counterparts.² Since catalysis primarily occurs at the surface, the overall activity of NPs strongly depends on both surface area and surface energy. These two factors are intrinsically related: increasing surface area exposes more active sites, while the surface energy can be modulated by controlling the exposed crystal facets. Extensive studies and comprehensive reviews have discussed how such surface structures dictate the catalytic performance of metal NPs across a broad range of reactions.³⁻⁷

Drawing parallels from biological systems, the catalytic efficiency of metalloenzymes is governed by the coordination environment of the metal co-factor, which is defined by both the immediate ligands and extended



coordination spheres that critically influence metal-site reactivity. Despite not being directly engaged in the catalytic cycle, these protein frameworks provide a microenvironment for the metal center, affecting local hydrophobicity, dielectric constant, and accessibility of specific reactants.⁸ This review seeks to summarize how ligands, particularly polymer ligands (see Section 2), attached to metal NP surfaces can similarly modulate catalytic performance, as electronic and steric regulators. Numerous studies have reported on “positive” ligand effects, where the presence of surface ligands enhances catalytic activity, even though these ligands often rearrange or exchange under reaction conditions. Much like the protein shell of an enzyme, these ligands influence catalysis by selectively facilitating substrate binding, stabilizing key intermediates, and directing product selectivity.⁹⁻¹³



Scheme 1. Illustrating the role of surface ligands in catalysis mediated by metal NPs.

In general, surface ligands on NPs play two principal roles (**Scheme 1**).¹⁴⁻¹⁷ First, they act as molecular gates, regulating access to the catalytic surface.¹⁵⁻¹⁷ In contrast to the uniform metal centers in homogeneous complexes, surface atoms on NPs display heterogeneous reactivity; atoms located at corners and edges are generally more active than those on flat terraces.³ Ligand coverage typically forms monolayers on specific facets (e.g., packing on lateral facets), which may reduce substrate adsorption on those regions and increase the accessibility on other sites. In case of polyhedral NPs, this selective exposure can suppress certain adsorption geometries (e.g., thiols on Pd to block the bridge site)¹⁸⁻²⁰ and consequently alter reaction selectivity. The “gate” effect can also extend beyond steric



blockage to include modulation of the interfacial microenvironment, through hydrophobicity, hydrogen bonding, or solvation, thereby influencing how substrates approach and transform at the catalytic surface.⁹⁻¹² Second, surface ligands can modify the electronic nature of surface atoms, similar to how donor–acceptor ligands tune transition-metal complexes in homogeneous systems.²¹⁻²³ Ligands with comparable steric effects but distinct binding motifs can yield markedly different catalytic outcomes by modifying local charge density (or the d band state of metal site).²⁴ Taking Pt supported on carbon (broadly used in organic synthesis for hydrogenation) as an example, interfacial electronic effects induced by ethylenediamine significantly modulate the hydrogenation of nitroaromatics, achieving nearly 100% selectivity for N-hydroxylanilines compared to only 33% with commercial Pt black.²⁵ The elevated surface electron density effectively stabilizes electron-deficient intermediates, thereby altering the hydrogenation selectivity. Overall, surface ligands can provide an alternative, post-synthetic approach for optimizing the catalytic behavior of metal NPs without re-synthesizing NPs.

2. Surface ligands in electrochemical CO₂ reduction reactions (eCO₂RRs)

The conversion of carbon dioxide (CO₂) into value-added chemicals has attracted considerable attention because it effectively promotes carbon cycling and reduces CO₂ emission.^{26, 27} CO₂ is thermodynamically stable due to its strong C=O bonds. Therefore, its activation requires substantial energy input and (multiple)electron transfers to overcome thermodynamic and kinetic barriers. To address this challenge, numerous CO₂ conversion strategies have been developed, including photochemical,²⁸ electrochemical,²⁹ thermochemical³⁰ and biochemical³¹ reduction pathways. Among these, electrochemical CO₂ reduction reaction (eCO₂RR) offers a pathway to zero-emission targets potentially by coupling with renewable electricity sources.³²⁻³⁵ CO₂ has +4 oxidation state of C and it can be reduced to a spectrum of products, such as CO, formic acid, methane, methanol, ethylene, ethanol and other products.³⁶⁻³⁸ Pioneered by Hori *et al.*,³⁹ many heterogeneous catalysts have been studied since the 1980s to activate CO₂ through electroreduction.⁴⁰⁻⁴³ In terms of their activity and selectivity, Group 11 noble metals like Au and Ag are among the most active catalysts for eCO₂RR. With a low density of reactive d-states, Au and Ag can coordinate CO₂ but have a weak binding with *CO, often enabling high selectivity toward CO (> 90%).⁴⁴⁻⁴⁶ Au in the forms of spherical NPs and nanoclusters can reduce CO₂ to CO with overpotentials of 300-450 mV.⁴⁷ AuNPs made from the reduction of thick Au oxide films even show an overpotential down to 150 mV as demonstrated by Kanan *et al.*⁴⁵,⁴⁸⁻⁵⁰ The p-block metals and their oxides, e.g., Sn and Bi, reduce CO₂ to formate with overpotentials > 1 V.⁵¹⁻⁵³ CO and formic acid that only require two electron transfers are kinetically favorable products and they can be prepared with high selectivity.⁵⁴⁻⁵⁶ CO also serves as a key intermediate for downstream synthesis coupled with the Fischer-Tropsch process.⁵⁷ Cu, on the other hand, has a high d band center and moderate binding affinity with *CO. It is the only catalyst capable of producing C₂ or hydrocarbon products,⁵⁸ known as more value-added compared to C₁ products, although it is not selective.



In all cases, hydrogen evolution reactions (HERs) compete with eCO₂RR because of their similar thermodynamic and kinetic barriers.⁵⁹ For commercial Cu foil, HERs reach >50% of Faradaic efficiency (FE, the percentage of electrons used towards a particular product).⁶⁰ To enhance eCO₂RR selectivity, suppressing HER is essential.⁶¹ Controlling structure and composition of nanocatalysts has been extensively used in the past to modulate their reactivity.^{3, 58, 62-65} For AuNPs, nanocubes with (100) dominated surface facets show a CO FE close to 94%, while octahedra with (111) facets have a CO FE about 50%.⁶⁶ Similarly, Cu (100) bound CO at a high coverage favors C–C coupling.⁶⁷ However, metal nanocatalysts are unstable under reductive potentials and irreversible structure dynamics bring challenges for their long-term applications. Alivisatos's group studied the morphological evolution of CuNPs during eCO₂RR.⁶⁸ 7 nm Cu spherical NPs grew into 23 nm after 10 min electrolysis at -1.25 V vs. reversible hydrogen electrode (RHE, the same hereafter unless otherwise noted). Similar results were reported by Yang's and Buonsanti's groups.^{69, 70} Buonsanti's group proposed the underlying mechanisms involved in the structural transformation of Cu-based nanocatalysts during eCO₂RR, including detachment, dissolution, Ostwald ripening, reshaping, fragmentation, agglomeration and poisoning.⁷⁰

Surface modification has emerged as an effective strategy to address these unmet challenges of nanocatalysts in eCO₂RR, although ligands have been overlooked as a catalytic barrier.^{11, 71-73} Recent results have recognized that surface ligands can enhance stability of nanocatalysts, provide selective binding and enhance local concentration of CO₂, as well as suppress the competing HER.⁷⁴⁻⁷⁷ Polymer ligands, with extended chain length, can effectively modulate the catalyst-electrolyte interface as an essential microenvironment to provide CO₂ capture, collectively improving CO₂ binding, the intermediates evolution and the products desorption.^{78, 79, 80} For example, incorporating FeNPs in porous ZIF-8 for eCO₂RR allows the porous layers to provide a hydrophobic environment for CO₂ adsorption and suppress HER, thereby achieving 90% of CO FE.⁸¹ Positively charged ligands can improve stability of intermediates during electrocatalytic cycles. Aminothiolate-coated Cu for eCO₂RR can promote initial CO₂ activation by the interaction between amine group and *CO₂.⁸² The amine group on the ligands can stabilize *COOH, as the intermediate from the first electron/proton transfer, through hydrogen bonding. As an extended coordination sphere, polymer ligands can also change the mass transport behaviors of ions, water and CO₂. In addition, polymers can present multiple binding motifs that strongly coordinate with metal NPs as compared to small molecular ligands, thereby preventing interparticle sintering under reaction conditions. For example, polymers having multiple N-heterocyclic carbene (NHC) moieties can significantly improve long-term stability of AuNPs^{83, 84} with an enhanced CO₂ selectivity.⁸⁵ Therefore, polymer ligands on catalysts show advantages in preventing the aggregation of catalysts in addition to modulating the electronic and steric structure.^{76, 77}



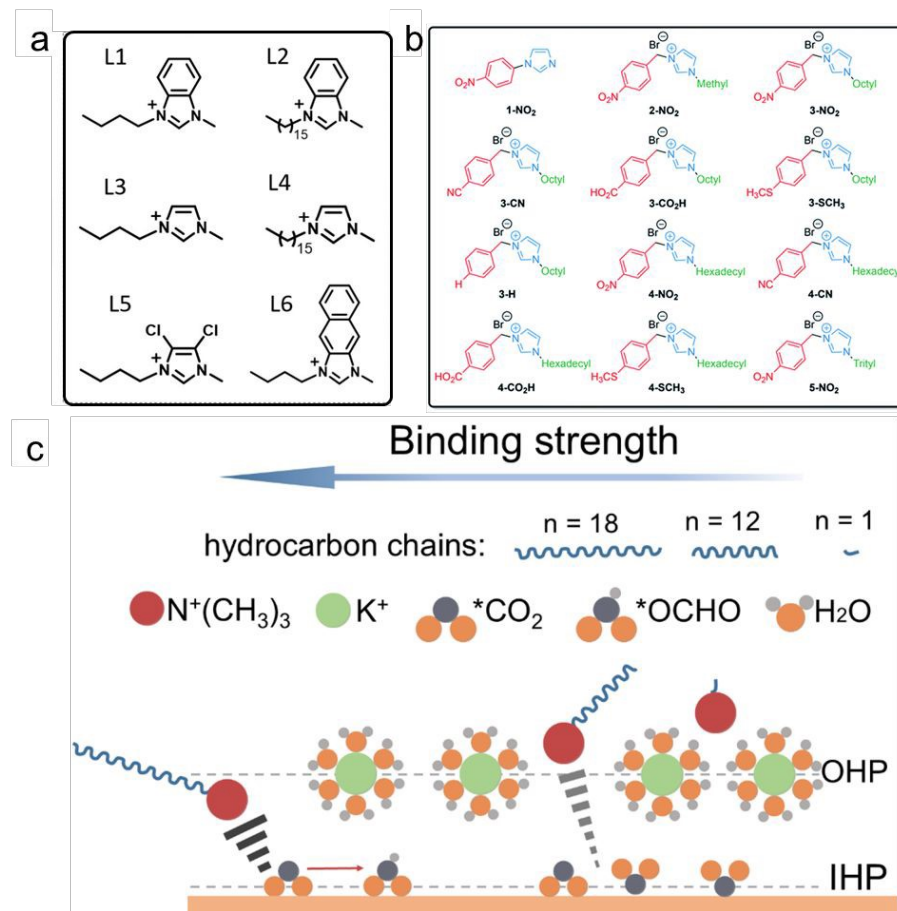


Figure 1. (a) Chemical structures of NHC ligands. Reproduced with permission.⁸⁶ Copyright 2025 American Chemical Society. (b) Chemical structures of imidazolium ligands with tunable anchor and tail groups. Reproduced with permission.⁸⁷ Copyright 2019 The Royal Society of Chemistry. (c) Schematic illustrating the steric effect of C_nTA⁺ cations with varying backbone lengths on modulating the binding strength of the intermediates. Reproduced with permission.⁸⁸ Copyright 2025 Wiley.

Electronic effects and hydrophobic effects as the two main mechanisms work synergistically to enhance eCO₂RR performance. Electronic effects mainly arise from the binding motifs that dictate the charge perturbation between the ligand and NP surface. The coordination of electron-donating or electron-withdrawing groups can also modify the d-band center of NPs, thereby influencing the affinity and stabilization of reactants and intermediates. Electron-donating ligands, such as amines and NHCs, have proven to facilitate the activation of electron-deficient species including CO₂,^{86,89} although the underlying mechanisms remain debated. For instance, in molecular NHC–Mn(I) complexes, CO₂ activation may proceed through different pathways: CO₂ can form adducts with the NHC,⁹⁰ or alternatively, the NHC can stabilize the formate (*COOH) intermediate via hydrogen bonding, which is generated after the first electron/proton transfer.⁹¹ Our group has investigated the effects of NHCs ligands on eCO₂RR using various NHCs with different electron-donating or -withdrawing groups modified gold NPs as catalysts (Figure



1a)⁸⁶ Compared with pure Au/C, the NHCs (L1) modified Au/C showed ~33% enhancement of partial current density for CO (J_{CO}), attributed to stabilization of *CO intermediates as confirmed by a shift of *CO vibrational frequency. However, the electronic nature of NHCs ligands had a limited effect on the eCO₂RR performance, and AuNPs with NHCs having electron-donating or -withdrawing groups showed similar reactivity for CO₂. Buonsanti and co-workers studied a family of imidazolium ligands with different functional groups and tail groups to promote the eCO₂RR (**Figure 1b**).⁸⁷ For oleylamine-modified silver nanocrystals (AgNCs), the H₂ FE is ~70% and CO FE is 29%. After modifying AgNCs with imidazole or imidazolium, the CO₂ selectivity dramatically improved. For example, the CO FE with imidazolium having *p*-NO₂ benzyl group (3-NO₂, **Figure 1b**) increases to 92%. Additionally, imidazoliums with other electron-withdrawing groups, *e.g.*, CN, CO₂H and SCH₃ benzyl groups all yielded much lower selectivity (CO FE 77%). In the absence of electron-withdrawing groups on the *p*-NO₂ benzyl group, the CO FE with 3-H (**Figure 1b**) was as low as 58%.⁸⁷

Hydrophobicity from the extended coordination sphere, although not directly involved in catalysis, can vary the microenvironment for eCO₂RR.⁹² Hydrophobic polymers create a nonpolar interfacial layer (*e.g.*, a few to tens of nanometers) that influences the local distribution of reactants, intermediates, and solvation near the catalyst surface. The eCO₂RR performance is often limited by the low solubility of CO₂ in the aqueous electrolyte in a typical H-cell. The limiting current density (j_{lim}) in eCO₂RR is proportional to the available CO₂ concentration. The local CO₂ concentration can be described as the surface adsorbed *CO₂ (θ_{CO_2}) as follows: $\theta_{CO_2} = \theta^* \cdot C_0 \exp(-E_{CO_2}/RT)$, where θ^* is the coverage of available surface sites, C_0 is the local CO₂ concentration, E_{CO_2} is the adsorption energy of CO₂ on the catalyst, R is the ideal gas constant, and T is the temperature.^{93, 94} By enriching CO₂ concentration at the catalytic interface, hydrophobic coatings can effectively improve selectivity while confining water molecules and protons. For example, Peters *et al.* coated Ag electrode with hydrophobic pyridinium-based additives, which highly suppressed HER and achieved CO FE > 99% due to the slow diffusion of protons through the hydrophobic layer.⁹⁵ Moreover, hydrophobicity also modulated the diffusion behavior of ions and gases, forming a confined reaction zone that favors multi-electron transfer processes. The degree of hydrophobicity is often tunable through alkyl chain length,^{96, 97} tail group structure, or polymer backbone design.^{96, 97} It determines how strongly the interfacial environment deviates from bulk electrolyte conditions. Sargent and co-workers utilized alkane-thiol modified copper nanoparticles (CuNPs) as catalysts.⁹⁷ Compared with pure CuNPs, the alkane-thiol modified CuNPs with chain lengths from C₂ to C₂₂ yield a higher FE to acetate. After optimizing the loading, coverage and chain length, the acetate FE reached 70% at 400 mA cm⁻². Density functional theory (DFT) calculations indicate that the ethylene intermediate (HOHC-CH₂O)* is more stable than the acetate intermediate (HOOC-CH₂)*, thus acetate is the main product. On the other hand, metal catalysts with intrinsic hydrophobicity that origin from their microstructures showed a high selectivity for CO₂ reduction. Yamauchi and co-workers coated Cu nanoneedles arrays with 1-octadecylthiol and obtained a superhydrophobic catalyst layer (water contact angle (WCA): 158.5°), achieving FE



(C₂+)⁹⁸ of 87% at -1.6 A cm^{-2} under acidic conditions.⁹⁸ Inspired by the hydrophobic structure of *Setaria*, Gao *et al.* developed a Cu needles array, which exhibited superhydrophobicity with WCA of 154°. The hydrophobic microstructure trapped a gas layer and enriched the local CO₂ concentration, enabling a high C₂+ production rate of 255 mA cm⁻² with a 64% FE.^{99 98, 100}

Compared with hydrophobic alkane-thiol ligands, hydrophobic ionic ligands, particularly quaternary ammonium cations (C_nT_A⁺), can promote the eCO₂RR performance by: i) stabilizing intermediates and repelling protons; and ii) enhancing the mass transport of CO₂ (**Figure 1c**).⁸⁸ After introducing octadecyl trimethyl ammonium chloride (C₁₈TAC) on CuNPs, the FE formate increased to ~70%, reaching a maximum of 90% at -0.8 V . For pure CuNPs, H₂ is the primary product (~55% at -0.8 V). The FE formate increases with the increase of alkyl chain length. The FE formate of C₁₈TAC modified CuNPs is 72.2%, that is 2.0, 2.9 times higher than those of C₁₂TAC, C₁TAC modified-CuNPs, respectively. The local hydrophobicity is therefore crucial in suppressing HER and promoting selectivity to CO₂ during eCO₂RR. Other than ammonium, benzimidazolium is another attractive ionic ligand that enhances eCO₂RR performance by modifying the interfacial electric field and buffering local pH in strongly acidic environments, achieving 80% FE (C₂+)¹⁰¹ at 100 mA cm⁻². The simulation results indicate that the surface electric field enables CO₂ activation in acidic media. Meanwhile, replacing alkali metal cations with benzimidazolium enhances the stability for over 150 h.¹⁰¹

Polymer ligands are fundamentally different from molecular ligands. Molecular ligands often form self-assembly monolayers (SAMs) on NPs. SAMs are typically dense and electronically insulating, thereby known as charge and ion insulators.¹⁰²⁻¹⁰⁶ On flat Au electrodes as an example, the SAMs of organothiols with long alkyl chains can block the access of redox species to the electrode.^{102, 103} The presence of pinhole defects, *e.g.*, shorter alkyl chains⁶⁵ or less flat surfaces,¹⁰⁷ allows the permeation of ionic species. As a result, NPs with polyhedral surfaces potentially bring more pinhole defects at the edge and corner sites where the redox species have access to the NP surface, compared to the flat metal electrode. On the other hand, polymer ligands, due to their large steric effect, do not form a dense layer, particularly through the “grafting to” approach. Typically, the grafting density of molecular thiols is about 3-9 per nm⁻²,¹⁰⁸ while, it is 0.1-0.5 per nm⁻² for polymers.^{109, 110} Their long chains therefore form a semi-permeable shell that allows the diffusion of small molecules/ions and reaction intermediates (**Figure 2a**). Our group has measured the interfacial mass transfer kinetics using three molecular redox probes, *i.e.*, ferricyanide, ruthenium hexaammine and ferrocenecarboxylic acid.¹¹¹ With molecular NHCs that form compact SAMs (**Figure 2b** and **c**), there is a dramatic decrease in redox current and apparent diffusion coefficient (D_0). In case of ruthenium hexaammine, D_0 dropped about three orders of magnitude, suggesting the slow ion transport limited to low-density pinhole defects within the SAM. In contrast, polymeric NHC ligands had a minor impact on D_0 ; and, in some cases, the increase of D_0 was observed for more hydrophobic probes, *e.g.*, ferrocenecarboxylic acid. These results suggest



that polymer ligands form a permeable interface for both small ions and larger redox probes (**Figure 2d**). Consequently, in eCO₂RR, where proton-coupled electron transfer dominates, hydrophobic polymer NHCs are unlikely to prevent the diffusion of hydrated ions.

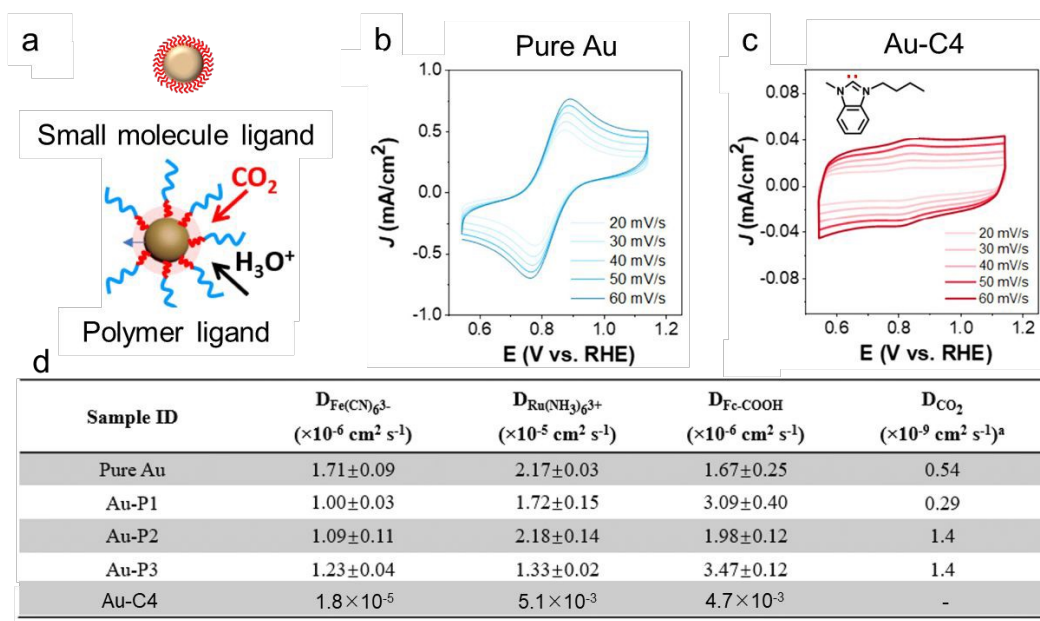


Figure 2. (a) Schematic illustration of small molecule and polymer ligand modified metal nanocatalyst for CO₂ and proton transport. Cyclic voltammetry scans of (b) AuNPs and (c) Au-C4 measured with 5 mM K₃Fe(CN)₆ at various scan rates. Reproduced with permission.⁸⁶ Copyright 2025 American Chemical Society. (d) Summary of diffusion coefficient (D) using various probe molecules including Fe(CN)₆³⁻, Ru(NH₃)₆³⁺, Fc-COOH, and CO₂. P1-P3: N-Heterocyclic carbene (NHC)-functionalized poly(ethylene oxide) (NHC-PEO·HCO₃⁻, P1), NHC-PS·HCO₃⁻ (P2), and block copolymer NHC-PEO-*b*-PS·HCO₃⁻ (P3). Reproduced with permission.¹¹¹ Copyright 2023 The Royal Society of Chemistry.

As discussed above, surface ligand modification plays a critical role in eCO₂RR and offers a promising way to tune the surface microenvironment of nanocatalysts. There are excellent reviews on the effects of binders on eCO₂RR,¹¹² ligand impact on heterogeneous electrocatalysis,⁷⁷ and ligand-modified catalysts for eCO₂RR.^{76, 80} None of these reviews specifically address polymer-modified nanocatalysts as a strategy for enhancing eCO₂RR performance. In the current review, we summarized the recent progress in polymer-modified metal nanocatalysts for eCO₂RR. We categorized polymer ligands into four types based on their functions: i) hydrophobic polymers, which control the mass transfer of CO₂ and hydrogen bonding network of water; ii) conductive polymers, which balance the conductivity and hydrophobicity; iii) ionic polymers, which stabilize the intermediates and vary the localized ion concentration, while synergically hydrophobic polymer backbones improve CO₂ reduction performance; and iv)

porous polymers, including metal-organic frameworks (MOF) and covalent-organic frameworks (COF), both of which offer high surface area and great potential to capture CO₂. We highlight current status and challenges in this rapidly evolving field. Continued progress in this area will not only deepen the mechanistic understanding of ligand effects in electrocatalysis but also accelerate the rational design of next-generation hybrid nanocatalysts for efficient and selective CO₂ conversion.

3. Hydrophobic polymer ligands for eCO₂RR

Nanocatalysts with suitable surface hydrophobicity can significantly regulate the product distribution of eCO₂RR. One effective strategy to adjust this hydrophobicity is the introduction of ligands. It is well-known that organothiols containing long alkyl chains reduce water wettability of metals.¹¹³⁻¹¹⁵ Cu dendrites modified with 1-octadecanethiol exhibit superhydrophobic behavior, showing a WCA as high as 153°, as demonstrated by Mougel and co-workers.¹¹⁶ The altered wettability modifies the electrolyte-electrode interface; with reduced water accessibility, stronger reducing potentials are required to drive CO₂ conversion (as summarized in **Table 1**). The hydrophilic Cu dendrite without 1-octadecanethiol only needed -0.68 V to reach a current density of -5 mA cm⁻², whereas its hydrophobic counterpart required -1.38 V. The hydrophobic Cu dendrites achieved notably improved selectivity, with FE ethylene of 56% and 17% for ethanol, compared to 9% and 4% for unmodified Cu under neutral conditions. Organothiols can form SAMs on many metal surfaces,⁶⁷ including all metals in Group 11, making them ideal for controlling surface hydrophobicity during eCO₂RR. Nevertheless, metal-thiolate binding is not electrochemically stable. For example, cyclic voltammetry or impedance spectroscopy studies suggest that the stability window of Au-thiolate monolayer in 0 V-1 V.¹¹⁷ Cu-thiolate is slightly more stable against reduction till -0.6 V.¹¹⁸ Under reductive conditions for eCO₂RR, the desorption of thiols likely occurs concurrently with or even before the reduction of CO₂.

Daasbjerg's group demonstrated that polymer hydrophobicity impacted the electrode-electrolyte interfaces in water during eCO₂RR on CuO electrode.¹¹⁹ With drop casting, hydrophobic poly(vinylidene fluoride) and polyethylene coatings (ca. 0.7-1 μM) enhanced the catalytic efficiency and CO₂ to C₂H₄ selectivity (32%, as compared to 16.7% for CuO at -1.12 V) by suppressing HER through high surface pH and restricted water diffusion; whereas coating with hydrophilic polymers, such as poly(vinylpyrrolidone), increased HER.



Table 1. Summary of polymer–metal hybrid nanocatalysts and their eCO₂RR performance

Polymer types	Advantages	Disadvantages	Materials	Water contact angle	Main product	FE _{product} (%)	FE _{H₂} (%)	J _{product} ^a (mA cm ⁻²)	E ^b (V)	Electrolyte	Cell type	Stability	Ref.
Hydrophobic polymers	Increasing local CO ₂ concentration	Poor conductivity	AuNPs/PVBMB-Im·HCO ₃ ⁻	-	CO	90	~10	-	-0.9	0.1 M KHCO ₃	H-cell	11 h	85
			AuNPs/NHC-PS-HCO ₃ ⁻	-	CO	~90	~10	21.2	-0.9	0.1 M KHCO ₃	H-cell	1 h	111
			AuNPs/PTFE	-	CO	94.7	~5	-	-0.7	0.25 M Na ₂ CO ₃	H-cell	3 h	120
			CuNPs/PTFE	145°	C ₂ +	95.4	~5	-	-1.6	1 M KOH	Flow cell	12 h	121
	Suppressing HER	Slowing down proton transfer	CuNWs/AuNWs/NHC-PS-HCO ₃ ⁻	-	C ₂ +	65	20	120	-1.1	0.5 M KHCO ₃	Flow cell	12 h	130
			CuO/FEP	144°	C ₂ +	52	22	37.4	-1.1	0.1 M KHCO ₃	H-cell	-	132
						62	8	220	-0.71	1 M KOH	Flow cell	16 h	132
			CuO/PAA	32°	C ₂ +	35	32	18	-1.1	0.1 M KHCO ₃	H-cell	-	132
						35	38	87.6	-0.71	1 M KOH	Flow cell	-	132
	Enhancing nanocatalysts' stability		CuO/Nafion	132°	C ₂ +	45	40	25	-1.1	0.1 M KHCO ₃	H-cell	-	132
						50	15	150	-0.71	1 M KOH	Flow cell	-	132
Conductive polymers	Improving electron transfer	Complex synthesis	CuNSs/PANI	-	C ₂ H ₄	58	~38	30.2	-1.2	0.1 M KCl	H-cell	10 h	134
			CuNPs/ABSA-PANI	142°	C ₂ +	81	~10	487	-2.6	1 M KCl (pH =1)	Flow cell	11 h	135
	Enhancing CO ₂ concentration	Poor adhesion and processing	CuPEDOT	-	CH ₄	62.7	~6	354	-1.58	1 M KOH	Flow cell	15 h	136
			PPy@HKUST-1	-	CH ₄	56	18	140	-0.8	1 M KOH	Flow cell	20 h	140
	Suppressing HER		PANI@HKUST-1	-	C ₂ H ₄	67.5	12	410	-0.9	1 M KOH	Flow cell	20 h	140
Ionic polymers	Enhancing CO ₂ solubility	Complex synthesis	CoTAPc/PFBr	69°	CO	98.6	-	22.5	-1.1	0.5 M KHCO ₃	H-cell	5 h	141
			CuNPs/PFSA/SSCD72	127°	C ₂ +	32	20		-1.1	0.1 M KHCO ₃	H-cell	-	147
	Adjusting CO ₂ /proton mass transfer	Poor conductivity	CuNPs/PFSA/SSCD79	134°	C ₂ +	34	16		-1.1	0.1 M KHCO ₃	H-cell	-	147
			CuNPs/PFSA/LSCD520	142°	C ₂ +	44	10		-1.1	0.1 M KHCO ₃	H-cell	-	147
			CuNPs/PFSA/LSCD521	146°	C ₂ +	32	8		-1.1	0.1 M KHCO ₃	H-cell	-	147
	Suppressing HER		CuNPs/PSImC ₁₆	~100°	CO	80	5	109	-1.2	0.1 M KHCO ₃	H-cell	9 h	148

			AuNPs/PS-quaternary ammonium	-	CO	94	6	41	-1.5	0.1 M KHCO ₃	H-cell	15 h	153
Stabilizing intermediates			CuNPs/pTPN-TMA	81°	C ₂ H ₄	21	42.5	-	-1.2	0.1 M KHCO ₃	H-cell	-	154
			CuNPs/pTPN-Pip	79°	C ₂ H ₄	8.7	52	-	-1.2	0.1 M KHCO ₃	H-cell	-	154
			CuNPs/pTPN-Py	82°	C ₂ H ₄	14	42	-	-1.2	0.1 M KHCO ₃	H-cell	-	154
			CuNPs/pTPN-Meim	67°	CH ₄	9	74	-	-1.2	0.1 M KHCO ₃	H-cell	-	154
			CuNPs/pTPN-Hexim	75°	C ₂ H ₄	21	55	-	-1.2	0.1 M KHCO ₃	H-cell	-	154
			CuNPs/pTPN-Beim	88°	C ₂ H ₄	46	18	331	-1.2	0.1 M KHCO ₃	H-cell	-	154
			AuNPs/Polyzwitterions (P6)	85°	CO	90	8	3.7	-0.8	0.1 M KHCO ₃	H-cell	-	156
			AuNPs/Polyzwitterions (P7)	16°	CO	70	28	-	-0.8	0.1 M KHCO ₃	H-cell	-	156
			AuNPs/Polyzwitterions (P8)	5°	CO	54	44	-	-0.8	0.1 M KHCO ₃	H-cell	-	156
			InNPs/c-PDDA	143°	HCOO ⁻	75	10	225	-1.6	0.4 M K ₂ SO ₄ (pH = 1)	Flow cell	36 h	157
			Cu@PIL	129°	CH ₄	42	16	111	-0.95	1 M KOH	Flow cell	24 h	158
Porous polymers	Improving CO ₂ concentration	Slowing down proton transfer	Cu ₂ ONPs/MOF	-	CH ₃ CH ₂ OH	44	20	9.7	-0.6	0.5 M KHCO ₃	H-cell	47 h	184
			CuNCs/MOF	-	C ₂ H ₄	50	16	-	-1.2	0.1 M KHCO ₃	H-cell	8 h	185
	Suppressing HER	Poor conductivity	2Bn-Cu@UiO-67	-	CH ₄	81	~5	420	-1.5	0.5 M KHCO ₃	Flow cell	2 h	188
			Cu ₂ O@CuHTTP	-	CH ₄	73	22	10.8	-1.4	0.1 M KCl/0.1 M KHCO ₃	H-cell	-	190
	Stabilizing intermediates		Cu/CeO ₂ /C	-	CH ₄	80	10	139	-1.5	0.5 M KHCO ₃	Flow cell	9 h	211
			AuNN@PCN	-	C ₂ H ₄	53	20	-	-1.2	0.1 M KHCO ₃	H-cell	10 h	213

^a J_{product} (mA cm⁻²): current density of products. ^b E (V): applied potentials E (V vs. RHE).

Polytetrafluoroethylene (PTFE), composed of densely fluorinated carbon chains, is a classic example of a highly hydrophobic polymer widely utilized to tailor electrode surfaces in eCO₂RR.¹²⁰⁻¹²² Its chemical inertness against redox reaction, low surface energy, and high crystallinity make it an ideal additive or coating material for improving catalytic performance and selectivity. AuNPs supported on carbon and mixed with PTFE showed a high CO FE of 94.7% at -0.7 V compared to ~88% of poly(vinyl alcohol) (PVA) modified AuNPs.¹²⁰ Porous PTFE nanocoating on CuNPs by physical mixing provided a high surface area for CO₂ transport, and high hydrophobicity increased the retention of CO from PTFE-covered Cu surfaces, achieving an FE (C₂₊) of 78% at 400 mA cm⁻².¹²¹ In addition, hydrophobicity could be introduced by simply mixing CuNPs with PTFE, which limited the interface with liquid electrolyte and enhanced local CO₂ concentration, achieving 2 times increase in single-pass conversion rate, in comparison with the electrode without PTFE.⁹³ Meanwhile, the finite diffusion layer thickness (δ), calculated from the electrochemical impedance spectra (EIS) using the equivalent impedance (Z_d), decreased from 20.2 to 3.2 μ m after mixing PTFE with nanocatalysts, indicating improved mass transport and CO₂ adsorption, thereby enhancing the FE (C₂₊).

N-Heterocyclic carbene (NHC)-functionalized polymers are believed to strengthen ligand coatings through forming covalent-like metal–carbon bonds (50–100 kcal mol⁻¹ for Group 10 and 11 metals).¹²³⁻¹²⁵ As strong σ -donor ligands, NHCs can effectively modulate the electronic structure of catalytic surfaces. Due to their exceptional binding affinity, NHCs can replace various native capping ligands on metal NPs, including thiols, thioethers, and oleates. However, free NHCs are typically highly reactive and unstable under air or moisture, which limits their direct use for modifying metal NPs synthesized in aqueous environments.



Figure 3. Two distinct methods for grafting NHC-functionalized polymer ligands onto metal NPs. (a, b) Scheme and photos showing the surface modification of AuNPs by PS-NHC-Cu(I) (a) and (b) NHC-PS-HCO₃⁻. Reproduced with permission.¹²⁶ Copyright 2020 The Royal Society of Chemistry.

Over the past few years, our group has developed two distinct “grafting-to” strategies for introducing NHC-functionalized polymer ligands onto metal NPs.¹²⁶⁻¹²⁹ The first approach relies on transmetalation, in which NHCs are initially generated through coordination with a sacrificial metal such as Cu(I) or Ag(I), forming stable NHC-Cu(I) and NHC-Ag(I) complexes. These intermediates can subsequently undergo transmetalation with metal NPs to yield robust polymer-NHC-metal linkages. NHC-functionalized polymers can be prepared via post-functionalization of polymers synthesized by atom transfer radical polymerization (ATRP). Typically, the terminal halogen group of the ATRP-derived polymer was first converted into an imidazolium or benzimidazolium moiety through alkylation with methylimidazole or methylbenzimidazole. Treatment of the resulting imidazole-terminated polymers with a mild bicarbonate base led to the formation of polymer-NHC-Cu(I) or polymer-NHC-Ag(I) complexes upon reaction with Cu₂O or Ag₂O.^{127, 128} These NHC–metal polymer ligands could be transferred onto citrate-capped metal NPs via biphasic ligand exchange at the water/toluene interface (~5 min), producing robust, polymer NHC-stabilized NPs (**Figure 3a**). The second approach involves direct *in situ* generation of NHCs without using a sacrificial metal.¹²⁶ In this method, imidazolium- or benzimidazolium-containing polymers undergo counterion exchange with bicarbonate, which deprotonates imidazolium to produce “free” NHCs while releasing CO₂ and water. The freshly generated NHCs, owing to their high reactivity, can immediately coordinate to metal NP surfaces, even in poor solvents for the polymers, within approximately 1 min (**Figure 3b**). Using these complementary ligand-exchange strategies, we have successfully prepared both monodentate and polydentate NHC-functionalized polymers with diverse backbones, including polystyrene, poly(meth)acrylate, and poly(meth)acrylamide, demonstrating broad applicability and versatility of the NHC-based surface modification approach.

Hydrophobic polymer-containing NHC ligands exert a pronounced influence on the selectivity of eCO₂RR. We prepared three types of monodentate NHC-functionalized polymer ligands: hydrophilic poly(ethylene oxide) (NHC-PEO·HCO₃⁻, P1), hydrophobic NHC-PS·HCO₃⁻ (P2), and amphiphilic block copolymer NHC-PEO-*b*-PS·HCO₃⁻ (P3) (**Figure 4a**).¹¹¹ These three polymer ligands were used to modify AuNPs supported on carbon, ensuring good electron conductivity between the electrode and the catalysts. The eCO₂RR performance was evaluated in 0.1 M KHCO₃ using an H-cell apparatus. Their performance was compared based on CO FE and their partial current density for CO (J_{CO}) and H₂ (J_{H_2}). As a control, the CO FE of Au/C varied in the range of 64% to 76% in the potential window of -0.7 to -1.1 V. The CO FE of Au-P2 and Au-P3 increased to about 90% in the same potential window; while the CO FE of Au-P1 was 80-85%, indicating hydrophobic PS enhanced CO₂-to-CO selectivity (**Figure 4b-e**). The J_{CO}/J_{H_2} ratio, as well as the CO/H₂ product ratio for Au-P2 and Au-P3 were 8.1 and 8.5, respectively, roughly 3 times higher than that of unmodified Au/C.



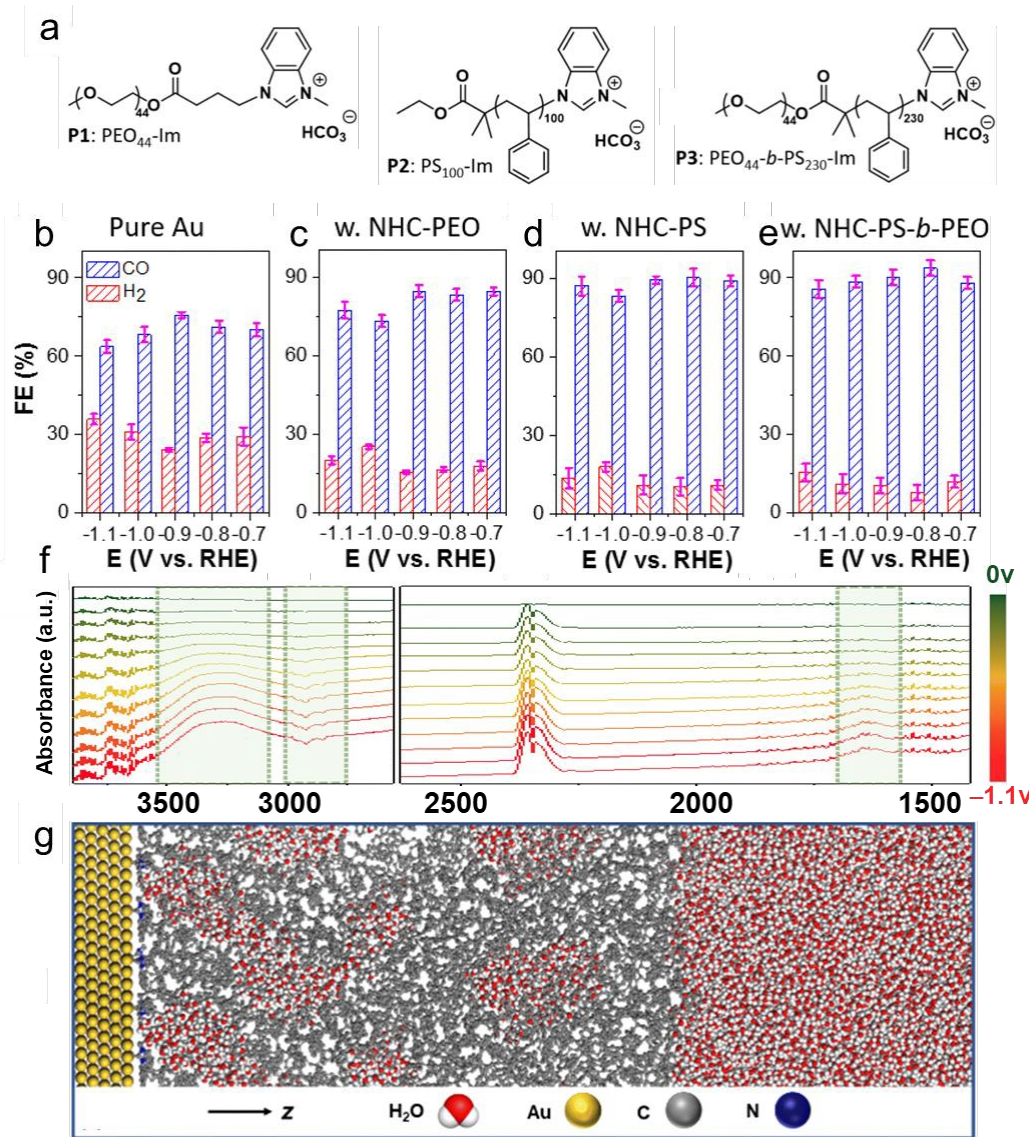


Figure 4. (a) Chemical structures of NHC-PEO·HCO₃⁻, (P1), NHC-PS·HCO₃⁻ (P2), and NHC-PEO-*b*-PS·HCO₃⁻ (P3). (b-e) CO and H₂ FE of Au (b), Au-P1 (c), Au-P2 (d) and Au-P3 (e). (f) In situ ATR-SEIRAS spectra of Au-P3, obtained at -0.3 V. (g) Molecular dynamics (MD) simulations showed the formation of water clusters at the catalyst-electrolyte interface. Reproduced with permission.¹¹¹ Copyright 2023 The Royal Society of Chemistry.

Comparable enhancements were demonstrated upon modification of gold nanowires (AuNWs) with hydrophobic NHC-PS·HCO₃⁻ for the eCO₂RR. After modification, the CO FE > 90% over an extended potential window (-0.4 to -1.0 V), whereas for unmodified Au NWs the CO FE > 90% only from -0.5 to -0.7 V. The in situ ATR-SEIRAS showed that ~41% of water formed clusters with PS-NHC modified Au NWs due to strong hydrogen bonding, as compared with ~10% for unmodified AuNWs, suggesting water was more confined for modified Au NWs. Meanwhile, the modified Au NWs behaved robust stability because of the strong bonding between NHC groups

with Au NWs, its CO FE maintained > 90% during 10 h electrolysis, while that of unmodified Au NWs dropped rapidly to 58% after 10 h test. In addition, the C_2H_4 FE reached 58% at -1.1 V by combining PS-NHC modified Au NWs with Cu NWs.¹³⁰

To probe the interfacial mass transport behavior, three different molecular probes were used to examine the mass transfer process at the catalyst-electrolyte interface. The diffusion coefficient (D_0) of anionic probe $K_3Fe(CN)_6$ and cationic probe $Ru(NH_3)_6^{3+}$ slightly decreased for Au-P1, Au-P2 and Au-P3, in comparison with Au/C. However, for Au-P1 and Au-P3, the D_0 of hydrated probe ferrocenecarboxylic acid (Fc-COOH) is two times higher than that of Au/C (**Figure 4d**). Those results suggest that polymer ligands had a minimum effect on the mass transport of small ions, including protons. Additionally, the diffusion coefficient of CO_2 for Au-P2 and Au-P3 was ~ 3 times higher than that of Au/C, due to the hydrophobic PS domains that provided high solubility for CO_2 . Attenuated total reflectance surface-enhanced infrared absorption spectroscopy (ATR-SEIRAS) confirmed that the polymer ligands did not inhibit water adsorption on the Au surface under negative bias. Notably, in the presence of hydrophobic polystyrene, the O-H stretching vibration of adsorbed water shifted to approximately 3300 cm^{-1} , from 3400 cm^{-1} for Au control without polymers, signifying enhanced hydrogen bonding interactions (**Figure 4f**). These spectral features indicate that, in the presence of hydrophobic PS ligands, water molecules became spatially confined at the catalyst-electrolyte interface, forming densely packed clusters with strengthened hydrogen-bond networks. Molecular dynamics (MD) simulations supported these findings, revealing a 5-fold increase in hydrogen-bond density near the hydrophobic PS domains (**Figure 4g**). Consequently, the reduced solubility of CO_2 within these water clusters promoted its preferential dissolution and enrichment in the hydrophobic polymer regions, thereby facilitating CO_2 activation and reduction at the interface.

Compared with monodentate NHC-functional polymer ligands, polydentate NHC-functionalized polymers showed higher stability due to the multiple binding motifs. Polydentate NHCs were synthesized through the quaternization of poly(vinylbenzyl chloride) with methyl benzimidazole (**Figure 5a**).⁸⁵ After exchanging counterion with bicarbonate, multi-NHC functionalized polymer (P4), consisting of poly(vinylbenzyl N-methylbenzimidazolium bicarbonate) (PVBMB-Im· HCO_3^-) and poly(vinylbenzyl N-methylbenzimidazolium carboxylate) (PVBMB-Im· CO_2^-) is air-stable and can be grafted to nanocatalysts under mild conditions (**Figure 5b**). After electrolysis at -0.9 V for 2 h, the electrochemically active surface area (ECSA) of Au-P4/C slightly decreased by 22.3%. In comparison, unmodified Au/C showed a larger loss, $\sim 75.3\%$ of its initial ECSA. The initial CO FE for Au-P4/C and Au/C were $\sim 90\%$ and 79%, respectively; while that of Au-P4/C decreased by $\sim 4\%$. However, the CO FE of Au/C decreased by $\sim 24\%$ after 2 h electroreduction, suggesting that Au-P4/C maintained stable CO selectivity (**Figure 5c**). The long-term stability was tested by chronoamperometry (i-t) at -0.9 V for 11 h. Au-P4/C showed only 14% current loss while unmodified Au/C exhibited $\sim 90\%$ current loss, suggesting the remarkable stability of



Au-P4. The structural stability of Au-P4/C was confirmed by TEM. For Au/C, large aggregates formed after 2 h reduction; while the AuNPs were much more stable for P1 modified AuNPs (**Figure 5d-g**).

Other than AuNPs, polydentate NHCs also were examined for commercial Pd/C. The commercial Pd/C catalyst had ultrasmall Pd about 3-5 nm and was not selective for eCO₂RR about 40% FE to CO. The selectivity of Pd-P4/C increased to 62% of CO and 3.5% of formate. The catalyst's stability improved remarkably after P4 modification. The ECSA loss of commercial Pd/C was 91.3%, while that of Pd-P4/C decreased by only 28.9% at -1.26 V for 2 h electrolysis. Hence, NHC-functionalized polymer ligands not only enhance NP stability but also leverage polymer hydrophobicity to facilitate CO₂ transport to the catalyst surface.

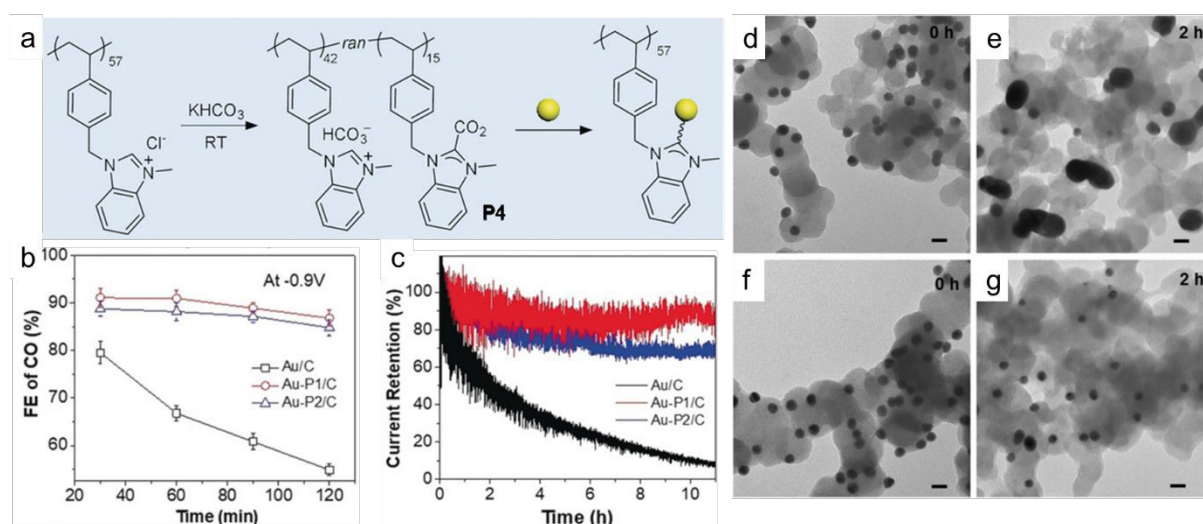


Figure 5. (a) Synthesis of polydentate NHC polymer with HCO₃⁻ as counterion (P4) and surface modification of NPs (yellow). (b) CO FE at -0.9 V for different electrolysis times. (c) Long-term stability plotted as current retention versus time at -0.9 V for 11 h. (d-g) TEM images of Au/C (d,e), Au-P4/C (f,g) before (left) and after (right) CO₂ reduction at -0.9 V for 2 h. All scale bars are 20 nm. Reproduced with permission.⁸⁵ Copyright 2019 Wiley.

Local hydrophobicity in eCO₂RR is important, but it does not require chemical grafting of polymers onto NPs. Polymer binders, for example, are often used to anchor catalysts onto electrode surfaces, ensuring mechanical stability, and efficient ion transport within electrochemical systems.¹³¹ In many cases, their properties influence the local reaction environment, particularly the wettability of catalysts against the electrolyte. Pham *et al.* studied different polymer binders: hydrophilic polyacrylic acid (PAA) and hydrophobic fluorinated ethylene propylene (FEP), Nafion to mix with CuO and prepared the electrode.¹³² The HER was suppressed with FEP and CuO-Nafion. The highest FE (C2+) of 52% was received on CuO-FEP at -1.1 V at a partial current density of 37.4 mA cm⁻²,

while the FE (C2+) of CuO-Nafion and CuO-PAA were ~43% and 35%, respectively. For hydrophilic Cu-PAA, the catalyst surface is fully wettable by the electrolyte, and the localized proton concentration is significantly higher, resulting in a substantially higher H₂ FE (~38% at -1.1 V). The hydrophobicity of these polymer binders was evaluated by using the WCA and the captive bubble contact angle measurements. The WCAs of CuO-FEP, CuO-Nafion, and CuO-PAA were 144°, 132° and 32°, respectively; while their captive bubble contact angles were 47°, 73° and 117°, respectively. By strategically manipulating surface wettability, one can modulate the local microenvironment, namely wettability of catalysts and transport rates of water, which are important for the competition between desired CO₂-reduction and unwanted HER pathways.

4. Conductive polymer ligands for eCO₂RR

Although typical hydrophobicity of polymers (e.g., PTFE) can enhance eCO₂RR performance by increasing local CO₂ concentration and suppressing HER, it also increases transfer resistance (i.e., the electrode to catalysts), leading to high cathode overpotential and low energy efficiency in eCO₂RR. To balance hydrophobicity and conductivity, one can physically mix nanocatalysts with conductive materials. For example, a superhydrophobic, highly conductive and hierarchical wire membrane consists of core-shell CuO NPs, carbon nanotubes and PTFE was prepared by thermal annealing of electrospun with PEO, Cu₂O NPs and PTFE NPs, labelled as CuO/F/C(w).¹³³ The eCO₂RR of CuO/F/C(w) was performed in a H-cell with CO₂ saturated 0.5 M KHCO₃ solution. Compared with 10.1% FE(C2-3) of bare CuO and 37.6% FE(C2-3) of the mixture of carbon nanotubes, Cu₂O NPs and PTFE NPs (CuO/F/C(m)), the maximum FE(C2-3) of CuO/F/C(w) is 56.8% at -1.4 V because of its excellent hydrophobicity/conductivity, highly exposed CuO NPs.

Conductive polymers are conjugated polymers with high electronic conductivity that modulate both conductivity (electrons and ions) and hydrophobicity.⁷⁸ A continuous electrodeposition can be used to coat various conductive polymers, e.g., polyaniline (PANI), polypyrrole (PPy), polythiophene (PTh), and their copolymers, together with metal catalysts (e.g., Cu, Pd, Zn, and Sn) on carbon paper (CP), serving as electrode for eCO₂RR (**Table 1**).¹³⁴ Taking Cu/PANI-CP (I) as an example, the 3D network of PANI nanofibers act as a matrix for electrodeposition of Cu nanosheets. Compared to conventional method, including drop-coating of CuNPs on PANI (Cu/PANI-CP (II)), drop-coating solvothermal synthesized CuNPs on PANI (Cu/PANI-CP (III)) and direct electrodeposition of CuNPs on CP (Cu-CP (IV)) (**Figure 6a**), Cu nanosheets were well-dispersed in PANI network that endow it with high ECSA, excellent eCO₂RR performance and improved long-term stability, as confirmed by the electrolysis of CO₂, which was carried out in CO₂-saturated 0.1M KCl using a H-cell. Cu/PANI-CP (I) had much higher C₂H₄ FE (~58% at -1.2 V) than other catalysts (**Figure 6b**). EIS indicated that the interfacial charge transfer resistance of Cu/PANI and PANI/CP was reduced or eliminated due to the well-contacted structure in Cu/PANI-CP (I). The film resistance between catalyst and substrate and charge transfer resistance between the electrolyte and Cu/PANI-CP (I) was much



smaller than these in other control catalysts (**Figure 6c**). As shown in **Figure 6d**, Cu/PANI-CP (I) balanced the fast electron transfer and CO_2 diffusion as a result of its well-dispersed Cu nanosheets and enhanced conductive network.

Similarly, Huang *et al.* fabricated Cu/PANI-CP by sequentially spray-coating of CuNPs and PANI on CP. The conductivity and hydrophobicity of PANI can be tuned via using various acids to modify PANI (**Figure 6e, f**), e.g. H_2SO_4 , *p*-aminobenzenesulfonic acid (ABSA) and dodecylbenzenesulphonic acid (DBSA), labelled as H_2SO_4 -PANI, ABSA-PANI, DBSA-PANI.¹³⁵ The distribution of relaxation time analysis on EIS data showed the lowest peak intensity for Cu/ABSA-PANI in low frequency region, demonstrating Cu/ABSA-PANI owned excellent electron and ion conductivity. Additionally, Cu/ABSA-PANI-CP behaved a lower internal resistance ($1.7\ \Omega$) than common hydrophobic molecules (PTFE, $6.7\ \Omega$ and SiC, $4.4\ \Omega$), significantly decreasing ohmic polarization and potential loss (**Figure 6g**). Acid-dopped PANI chains also exhibited much lower interfacial electron transfer resistance than PANI. In comparison with H_2SO_4 -PANI and DBSA-PANI, the strong steric hindrance effect of ABSA resulted in PANI chains becoming more extended, leading to higher conductivity and lower charge transfer resistance. Meanwhile, the hydrophobicity of PANI was well-remained for ABSA-PANI with a WCA of 142° (**Figure 6h**). The eCO₂RR were performed in a mixture of 1 M KCl and 0.05 M H_2SO_4 (pH = 1). The maximum FE (C2+) of Cu/ABSA-PANI-CP reached 81% at $600\ \text{mA cm}^{-2}$, higher than Cu-CP ($\sim 34\%$) and Cu/ABSA-PANI-CP ($\sim 70\%$) (**Figure 6i**). Meanwhile, Cu/ABSA-PANI-CP was stable over 11 h at $600\ \text{mA cm}^{-2}$ with FE (C2+) $> 60\%$. After modification by acids, Cu/ABSA-PANI-CP adsorbed 2.1 times more K⁺ than Cu-CP because of the electrostatic interaction between $-\text{SO}_3^-$ and K⁺, resulting in high performance at low concentration of alkali cations. The CO₂/Ar partial pressure experiment and DRT analysis on the EIS data indicated Cu/ABSA-PANI-CP was insensitive to the variation of CO₂ concentration, suggesting ABSA-PANI polymer layer is conducive to CO₂ adsorption and maintains a high local CO₂/H₂O concentration ratio, thereby facilitating the eCO₂RR. Compared with hydrophobic polymer (PTFE, $-3.5\ \text{V}$) or hydrophobic coating (SiC, $-3.3\ \text{V}$), it is required only $-2.6\ \text{V}$ for Cu/ABSA-PANI to reach a current density of $600\ \text{mA cm}^{-2}$ (**Figure 6j**), suggesting conductive PANI improves the energy efficiency.



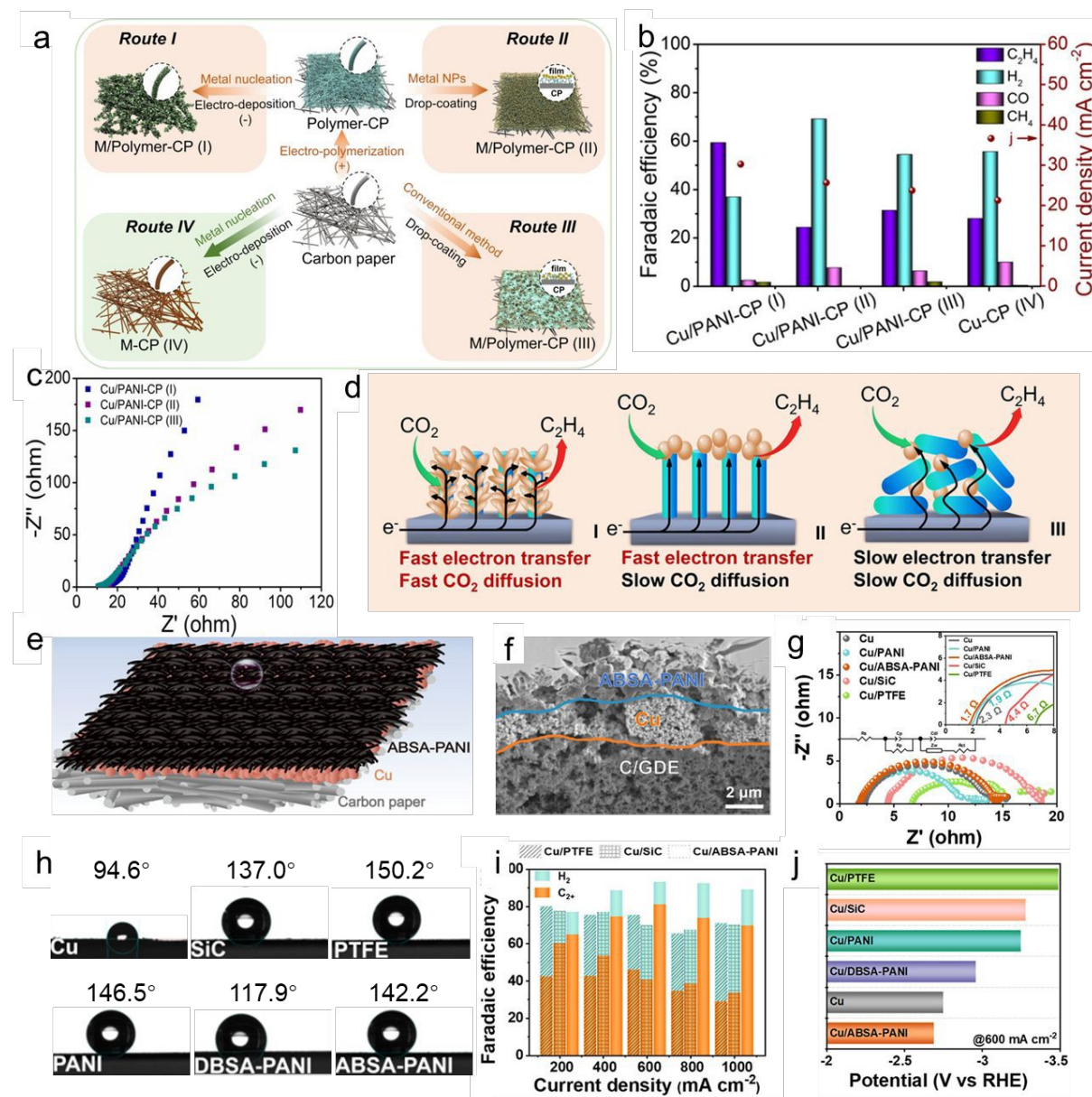


Figure 6. (a) Process used to prepare various electrodes. (b) Product distribution and average current density over different electrodes. (c) Nyquist and plot of Cu/PANI-CP (I), Cu/PANI-CP (II), and Cu/PANI-CP (III) electrodes in CO₂-saturated 0.1M KCl solution at equilibrium potential for eCO₂RR. (d) CO₂ diffusion and electron transfer on various Cu/PANI-CP electrodes with different structures. Reproduced with permission.¹³⁴ Copyright 2021 Wiley. Scheme (e) and cross-sectional SEM image (f) of the ABSA-PANI/Cu/C electrode. Water contact angle (g) and Nyquist plots (h) of Cu, SiC, PTFE, PANI, DBSA-PANI, ABSA-PANI. (i) Comparison of product distribution for Cu/PTFE, Cu/SiC, and Cu/ABSA-PANI in flow cells with 0.05 M H₂SO₄ and 1 M KCl. (j) Comparison of voltages consumed by different electrodes to achieve 600 mA cm⁻². Reproduced with permission.¹³⁵ Copyright 2025 Wiley.



Poly(3,4-ethylenedioxythiophene) (PEDOT) is another widely used conductive polymer and it is commonly employed as a flexible electrode material in organic electronics.¹³⁶⁻¹³⁸ Meanwhile, the thiophene (Th) of EDOT units can coordinate with other metal ions, enabling the construction of metal–polymer hybrid catalysts. Han *et al.* prepared a novel layered coordination polymer (Cu-PEDOT) through in situ redox polymerization of EDOT and copper chloride. As a weak oxidant, Cu²⁺ drove the polymerization of EDOT while Cu²⁺ was trapped in PEDOT particles with a Cu to S ratio of 1:1.2. The hybrid catalysts had a high conductivity of 6×10^{-2} S m⁻¹.¹³⁹ In a three-compartment flow cell with 1 M KOH, Cu-PEDOT showed a CH₄ FE of 62.7% at -1.58 V, about 1.6, 2.1, and 2.4 times higher than that of CuO (39.1%), CuS (0.3%), and Cu (26.3%). DFT calculations suggested that the d-band center of Cu-PEDOT had a 0.4 eV positive shift, as compared to that of pure Cu, leading to favorable adsorption of *CO. The strong binding of *CO promoted the deep reduction to CH₄ along with the exothermic steps of *CO₂ to *COOH (-1.04 eV) and *CO to *CHO (-0.51 eV).

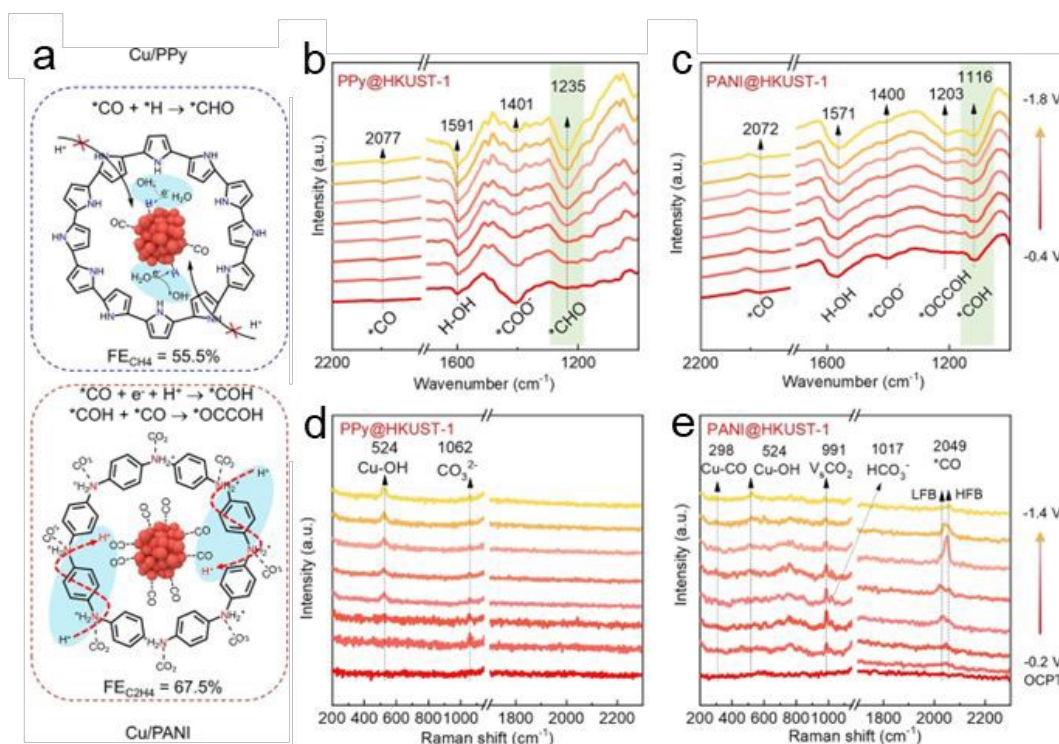


Figure 7. (a) Proposed mechanism for the MOF-derived Cu/PPy and Cu/PANI interfaces to steer the eCO₂RR pathway. ATR-SEIRAS spectra of (b) PPy@HKUST-1 and (c) PANI@HKUST-1. Raman spectra of (d) PPy@HKUST-1 and (e) PANI@HKUST-1 during eCO₂RR. Reproduced with permission.¹⁴⁰ Copyright 2023 Wiley.

In addition, the selectivity of eCO₂RR can be varied by proton shuttling mechanisms in conductive polymers. With PANI and PPy impregnated Cu-based MOF (HKUST-1), CH₄ was the main product for PPy@HKUST-1 with a

maximum FE of 55.5% at 250 mA cm⁻², while C₂H₄ is the main product for PANI@HKUST-1 with an FE of 67.5% at 600 mA cm⁻², in comparison to HKUST-1 with a CO FE of 67.5% at 600 mA cm⁻² at 100 mA cm⁻² (**Figure 7a**).¹⁴⁰ In attenuated total reflection surface enhanced infrared spectroscopy (ATR-SEIRAS), for PPy@HKUST-1, the intensity of H-OH bending (1591 cm⁻¹) and H-C=O stretching (1235 cm⁻¹) of *CHO synchronously enhanced with the increase of reduction potential, indicating that, i) *CHO formed by coupling *CO and *H; and ii) *CHO mediated the formation of CH₄. For PANI@HKUST-1, apart from the common intermediates of *CO (2072 cm⁻¹) and *COO⁻ (1400 cm⁻¹) observed for PPy@HKUST-1, a strong peak of C=O stretching is showed at 1116 cm⁻¹ (**Figure 7b, c**), attributed to *COH. In addition, the peak intensity at 1203 cm⁻¹, assigning to *OCCOH, increased with potential. The intensity of H-OH bending showed no significant increase with potential, suggesting that the high *CO coverage led to the asymmetric coupling of *COH and *CO. The further operando Raman spectroscopy also confirmed high *CO coverage for PANI@HKUST-1, evidenced by peaks at 298 cm⁻¹ (Cu-CO rotation) and 2033-2049 cm⁻¹ (C≡O stretching) (**Figure 7d, e**). In comparison, PPy@HKUST-1 exhibited Cu-OH species at 524 cm⁻¹. DFT calculations suggested that PPy@HKUST-1 showed a much lower activation barrier for surface *H formation (0.57 eV) than PANI/Cu (1.63 eV), enabling easier protonation of adsorbed *CO to *CHO, which favors CH₄ formation at moderate to low *CO coverage. The proton shuttling via benzenoid -NH- on PANI/Cu has a favorable barrier (0.53 eV) and small free energy change (0.15 eV) for reducing *CO to *COH, using protonated -NH₂⁺ as the hydrogen source, whereas O-protonation of *CO is less favorable (2.1 eV), aligning with observed *COH formation and subsequent coupling to OCCOH and further hydrogenation to C₂H₄.

5. Ionic polymer ligands for eCO₂RR

Ionic polymers, which balance ionic functionality and hydrophobicity to modulate interfacial ion conductivity and water accessibility, have also attracted much attention for eCO₂RR. By precisely tuning the content and distribution of ionic groups within the polymers, one can control those interfacial properties. A higher density of ionic groups enhances proton or water transport through ion-dipole interaction, whereas incorporating hydrophobic segments can facilitate CO₂ diffusion. Ye *et al.* designed the positively charged polyfluorene (PF) with covalently grafting cobalt tetraaminophthalocyanine (CoTAPc) through the successive reaction between CoTAPc/trimethylamine (TMA) and bromoalkyl polyfluorene (PFBr) (**Figure 8a**).¹⁴¹ The positively charged backbones the microenvironment near the active sites were thought to lower the proton concentration. In a H-cell test, the CO FE and J_{CO} of PF-CoTAPc reached 98.6% and -22.5 mA cm⁻² at -0.8 V, while the CO FE and J_{CO} of CoTAPc were 90.8% and -13.7 mA cm⁻². The CO production rate (TOF_(ICP)) of PF-CoTAPc was 2.0 s⁻¹ at -0.8 V, higher than that of CoTAPc (1.2 s⁻¹). Given the well-dispersed active Co sites within ionic polymers, the surface accessible Co sites of PF-CoTAPc were about 1.6 times that of CoTAPc. In a bipolar membrane (BPM) electrolyzer, the PF-CoTAPc also showed a CO FE of 82.6% at 100 mA cm⁻², as compared to that of CoTAPc, ~69.3% (**Figure 8b-d**).

Rotating disk electrode (RDE) voltammetry, measured in the N_2 -saturated 0.05 M H_2SO_4 with 3 M KCl electrolyte, showed typical diffusion limiting current in the range of -0.9 to -1.6 V (Figure 8e). A much smaller HER current for PF-CoTAPc was seen, as compared to that of CoTAPc and PFBr-CoTAPc. Hydrophobic PF-CoTAPc obviously limited proton diffusion. To minimize the impact of K^+ known to enhance eCO₂RR performance due to the ion repulsion between K^+ hydrates and protons (Figure 8f), the eCO₂RR was further carried out in 0.05 M H_2SO_4 with 0.01 M KCl. PF-CoTAPc still reached the highest CO FE at a lower overpotential in comparison with the other two catalysts. Those results suggested that the HER was suppressed by the quaternary ammonium groups to improve the overall selectivity of eCO₂RR under acidic conditions (Figure 8g).

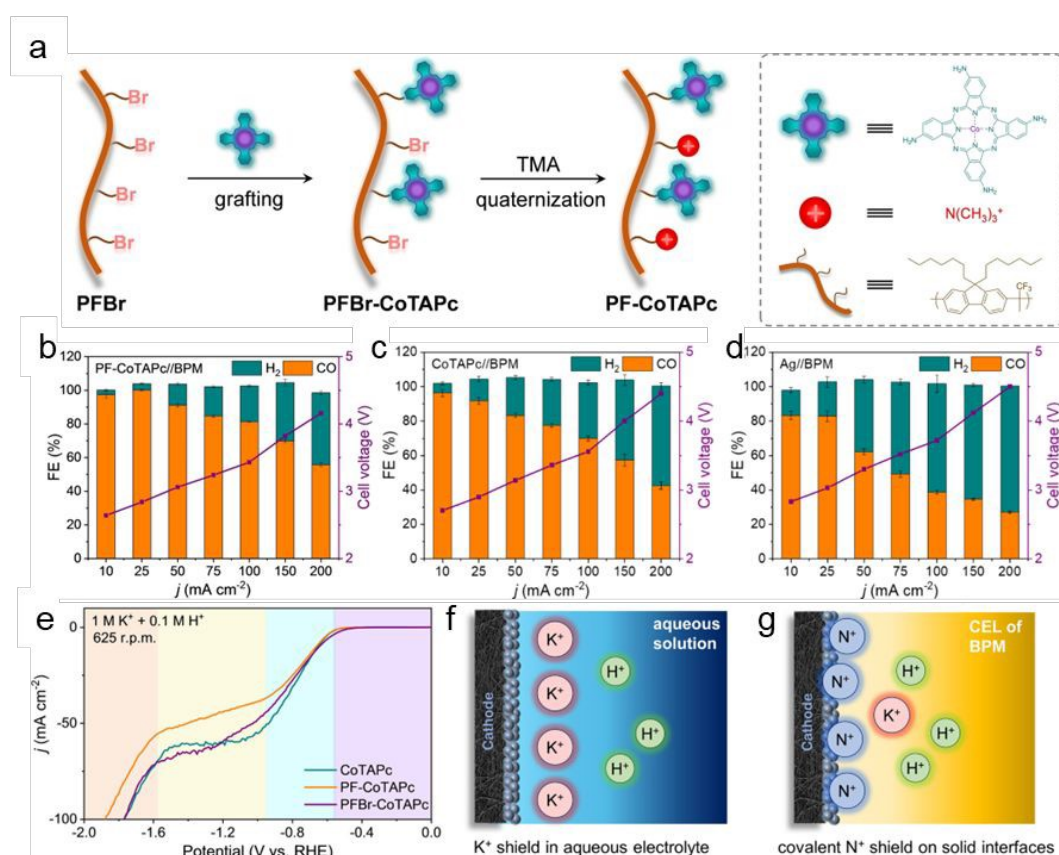


Figure 8. (a) Synthesis of polymeric catalyst PF-CoTAPc. (b-d) CO, H_2 FE and cell voltage of PF-CoTAPc (b), CoTAPc (c) and Ag (d) in BPM-based zero-gap electrolyzer. (e) LSV curves collected at a scan rate of 40 mV s^{-1} in N_2 -saturated solutions (1 M K^+ and 0.1 M H^+) at rotating speeds of 625 r.p.m. (f, g) Illustration of local fields at the diffusion layers for (f) conventional method with high-concentration alkali metals and (g) covalent grafting of quaternary ammonium groups. Reproduced with permission.¹⁴¹ Copyright 2024 Wiley.

The incorporation of ionic polymers as binders has proven equally critical for optimizing the performance of metal NPs. As aforementioned, ionic polymers actively modulate the interfacial microenvironment surrounding catalytic



surface. Ionic polymers contain different charged groups, such as sulfonate, quaternary ammonium, or imidazolium moieties, that create ion-selective domains at the electrode–electrolyte interface. These charged regions govern the transport of reactive species, including protons, hydroxide ions, and bicarbonate, and can drastically influence the competition between CO_2 reduction and HER. For example, polycations, including commercially available Sustainion, containing quaternary ammonium or imidazolium groups, favor the accumulation of bicarbonate and hydroxide anions near catalysts. For example, Bell and co-workers used Sustainion (ammonium) and Nafion (sulfonate) to construct ionic bilayers on the Cu surface to regulate pH, local water and CO_2 concentration. With the coating of both ionomers, 80% FE (C_2H_4) at -1.15 V .¹⁴² The anionic Nafion enhanced CO_2 transfer, while the cationic layer increased the local pH and both layers changed water concentration. In a related study, Ngene *et al.* used Cu_2O nanocubes as model catalysts and mixed them with Sustainion or Nafion as a binder, and compared their catalytic behaviors.¹⁴³ Five electrodes were prepared by mixing Cu_2O nanocubes with Nafion or Sustainion, including no binder (as control), Nafion, Sustainion, Naf-Sus and Sus-Naf (note: Naf-Sus indicates two layers: the first layer is Cu_2O nanocubes with Nafion, the last layer is pure Sustainion; and *vice versa*). The e CO_2 RR results showed that all electrodes containing Nafion had a low H_2 FE and high FE towards C_2H_4 due to suppressing HER and promoting e CO_2 RR activity. The presence of cationic polymer binder enhanced the ratio of ethanol to ethylene. For Cu_2O nanocubes without a binder, the reduction of protons or H_2O resulted in the accumulation of OH^- . It served as a proton acceptor from bicarbonate which buffers the local pH by reacting with OH^- to form CO_3^{2-} ; while K^+ balanced negatively charged species that improve the water-mediated HER and e CO_2 RR. On the other hand, the positively charged Sustainion favored bicarbonate anions and repel K^+ , resulting in bicarbonate precipitation in the Sustainion layer. Hence, the ECSA, current density and C_2H_4 selectivity showed a large decrease of 43%, 66% and 50% after 20 h electrolysis. However, the negatively charged sulfonate of Nafion blocked OH^- and CO_3^{2-} transport, and increased the abundance of K^+ , thereby suppressing HER. Similarly, the effect of charged polymer binders among Nafion, Sustainion and anion-exchange polymer binder with methylimidazolium groups (PiperION) on e CO_2 RR was compared using AgNPs as catalysts.¹⁴⁴ Compared to binder-free AgNPs, the H_2 FE and HCOO^- FE of Nafion coated AgNPs increased 3~4%, while HCOO^- FE of Sustainion coated AgNPs increased 6.6%. Among three binders, the H_2 FE of PiperION coated AgNPs increased by 15.9% due to hydrophilicity. Sustainion coated AgNPs had the lowest ECSA yet it behaved the best e CO_2 RR with a CO FE of > 99% because of the improved CO_2 availability.

Perfluorinated sulfonic acid (PFSA) is a typical hydrophobic/ionic polymer, which efficiently improve CO_2 and ion mass transfer. The Sargent's group demonstrated that PFSA ionomers coated Cu catalysts were highly selective for CO_2 reduction (> 90% with 65%~75% to C_2H_4).¹⁴⁵ The hydrophobic $(\text{CF}_2)_n$ domains on Cu surface provided continuous percolating hydrophobic pathways for the diffusion of non-polar gas reactants while limiting the access of protons/water. This drawback is not critical in flow-cell reactors, where the catalyst layer is thin and gas diffusion



occurs efficiently over micrometer-scale distances. In contrast, in traditional H-type reactors with limited mass transport, excessive hydrophobic coating can severely restrict both electron transfer and ion access to the catalyst surface, significantly slowing down the electroreduction process.¹¹⁶ Furthermore, PFSA has a good selectivity for CO₂ mass transport from PFSA to nanocatalyst surface.¹⁴⁶ Particularly, the local CO₂ and H₂O mass transfer can be tuned by varying the side-chain lengths of PFSA. For example, Wang *et al.* achieved precise regulation of CO₂/H₂O ratios by incorporating CuNPs with PFSA ionomers containing tunable side-chain lengths.¹⁴⁷ The DFT calculations suggested that PFSA with long side-chain (LSC-PFSA) own higher binding energy with H₂O and lower binding energy with CO₂, suggesting a stronger CO₂ affinity, compared with PFSA with short side-chain (SSC-PFSA). As the increase of side-chain lengths, the hydrophobicity of PFSA ionomers increases. Meanwhile, the hydrophobicity decreases as the increase of the ratio of catalyst and ionomer (C/I ratio) decreases. The improved CO₂ capability and suppressed H₂O transport led to 89.4% FE(C₂⁺) at 536 mA cm⁻² for LSC-PFSA. In situ ATR-SEIRAS indicated that LSC-PFSA showed an obvious *CO signal (~2060 cm⁻¹) at a lower potential and relatively low H₂O signal (~3500 cm⁻¹), compared with SSC-PFSA, suggesting the enhanced CO₂ transfer and suppressed H₂O.

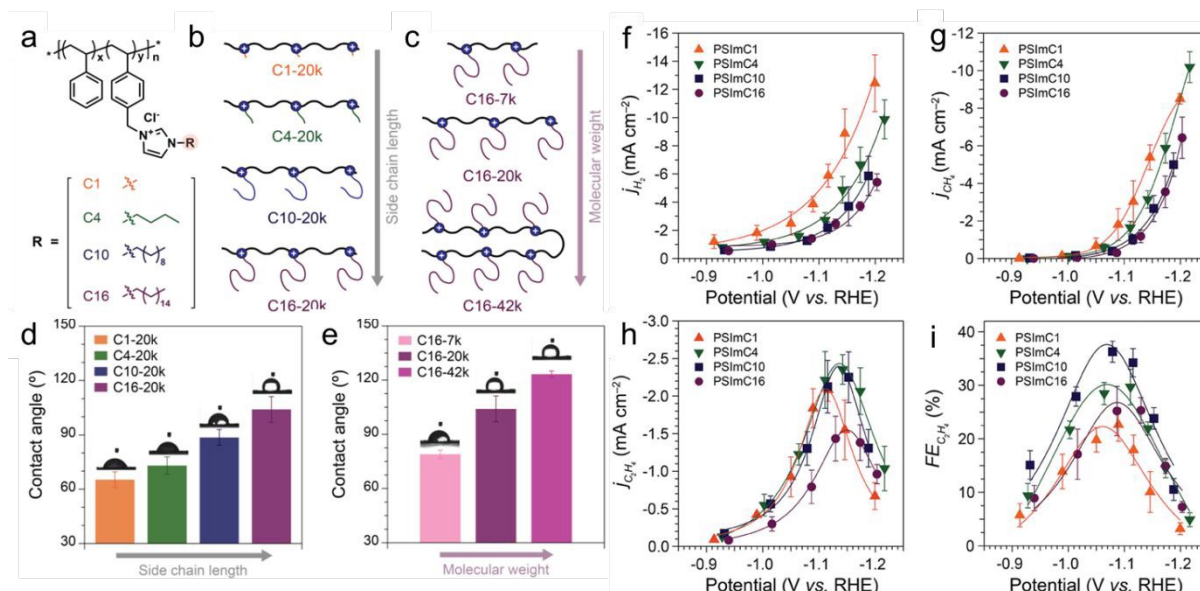


Figure 9. (a) Chemical structures of 1-*n*-alkylimidazolium ionomers with *n*-alkyl side chains of varying lengths: methyl (C₁), *n*-butyl (C₄), *n*-decyl (C₁₀), and *n*-hexadecyl (C₁₆). (b, c) Schematic illustrations of ionomers with systematic variations in (b) side chain length (C₁-, C₄-, C₁₀-, and C₁₆-20k) at a fixed molecular weight of 20 kg mol⁻¹ and (c) molecular weight (C₁₆-7k, C₁₆-20k, and C₁₆-42k) at a fixed alkyl side chain length of C₁₆. Contact angles of PSIm with (d) longer alkyl side chains and (e) higher molecular weights of the ionomers. Partial current densities for H₂ (f) CH₄ (g) and C₂H₄ (h) during eCO₂RR at different applied potentials in a CO₂-saturated 0.1 M KHCO₃. (i) C₂H₄ FE measured after electrolysis for 1 h. Reproduced with permission.¹⁴⁸ Copyright 2025 American Chemical Society.

On the other hand, positively charged polymers with similar structural features to Sustainion can serve as binders for metal nanocatalysts because of their ion conductivity. The hydrophobic–hydrophilic balance determines how water and CO₂ molecules access the catalyst surface, directly impacting catalytic efficiency. The copolymer of poly(styrene-*co*-4-vinylbenzyl chloride) (PS-*co*-4VBC) can be converted to a positively charged ammonium using alkylation, e.g., 1-n-alkylimidazolium. The impacts of side chain lengths and molecular weight of positively charged polymer binders has been systematically studied by Koh and colleagues (**Figure 9a-c**).^{148, 149} WCAs increased from 65° for C₁-20k to 104° for C₁₆-20k and reach 123° for C₁₆-42k (**Figure 9d, e**). The imidazolium functionalized PS-*co*-4VBC with different *n*-alkyl side chains (PSImC_n = 1, 4, 10, and 16) were synthesized and these polymer binders were mixed with commercial CuNPs and eCO₂RR was conducted in a H-cell using CO₂-saturated 0.1 M KHCO₃ as electrolyte. The results showed that both HER and CH₄ production were hindered with as side chain length increased. For example, the J_{H_2} of Cu-PSImC₁₆ decreased by 56.5% at -1.20 V, and J_{CH_4} of Cu-PSImC₁₆ shifted from -3.0 to -1.2 mA cm⁻² at -1.13 V, compared to those of Cu-PSImC₁ (**Figure 9f, g**). However, the peak of $J_{C_2H_4}$ increases by 13.0% from Cu-PSImC₁ to Cu-PSImC₄ and Cu-PSImC₁₀ and then decreases by 36.2% from Cu-PSImC₁₀ to Cu-PSImC₁₆, indicating PSImC₁₀ with optimized chain length for C₂H₄ selectivity (**Figure 9h, i**). DFT calculations suggested that imidazolium moieties and the larger steric bulk of the long alkyl side chains hindered the interaction between the Cu (111) surface and protons, thereby decreasing the *H surface coverage and slowing HER kinetics. The *CO intermediate was more stable than the *HCO intermediate with the increase of chain lengths. Meanwhile, the activation energy of the proton coupled electron transfer (PCET) step was impeded, leading to the restricted overall kinetics of the CH₄ formation. Contrastingly, the *2CO state was more stable with increasing alkyl chain length, facilitating the reaction kinetics of C–C coupling for C₂H₄ formation. A hydrophobic environment provided by PSImC_n with long side chains led to a lower local water concentration and an increase of CO₂ and the *CO intermediate, hence suppressing HER and CH₄ production. Moreover, polymer chain lengths also had a role in controlling over the selectivity of CO₂ reduction. Using PSImC₁₆ modified AgNPs (molecular weight of polymer chains are 7-42 kg mol⁻¹), PSImC₁₆ with 20 kg mol⁻¹ had the highest selectivity to C₂H₄ with an FE of 52.4%, due to the suitable ion dissociation and polymer segmental mobility.

Quaternary ammonium groups are excellent binding motifs for metal NPs and they have been extensively used in the design of polyhedral NPs.¹⁵⁰⁻¹⁵² Our group designed polymer ligands with ammonium head groups and demonstrated those polymers could modify various metal NPs.¹⁵³ The synthesis of such polymer ligands made use of alkylation of halogen-terminated polystyrene (PS) prepared via ATRP with N,N,N',N'-tetramethylethylenediamine, followed by further quaternization of their tertiary amines with iodomethane. Those bidentate polymers (P5, **Figure 10a**) with two ammonium head groups could modify citrate-capped metal NPs through biphasic phase transfer by mixing aqueous metal NPs with a toluene solution of P5. Such quaternary-



ammonium containing hydrophobic polymers can introduce an ionic layer at the catalyst–electrolyte interface. In CO_2 electrolysis (H-cell, 0.1 M KHCO_3), unmodified Au/C exhibited CO FE 50–70% from -0.8 to -1.3 V, falling to 38% at -1.5 V due to mass-transport limitations by the low CO_2 solubility. In contrast, Au/C modified with P5 maintained >94% CO FE even at -1.5 V, with a continuously increasing partial CO current density J_{CO} of ~ 41 mA cm^{-2} and nearly constant H_2 partial current J_{H_2} of ~ 7 mA cm^{-2} (Figure 10b, c). Quaternary ammonium-functionalized polymer ligands with a thin-layer of ionic head groups can significantly improve both CO_2 reduction selectivity and catalyst durability through interfacial stabilization and local environment modulation.

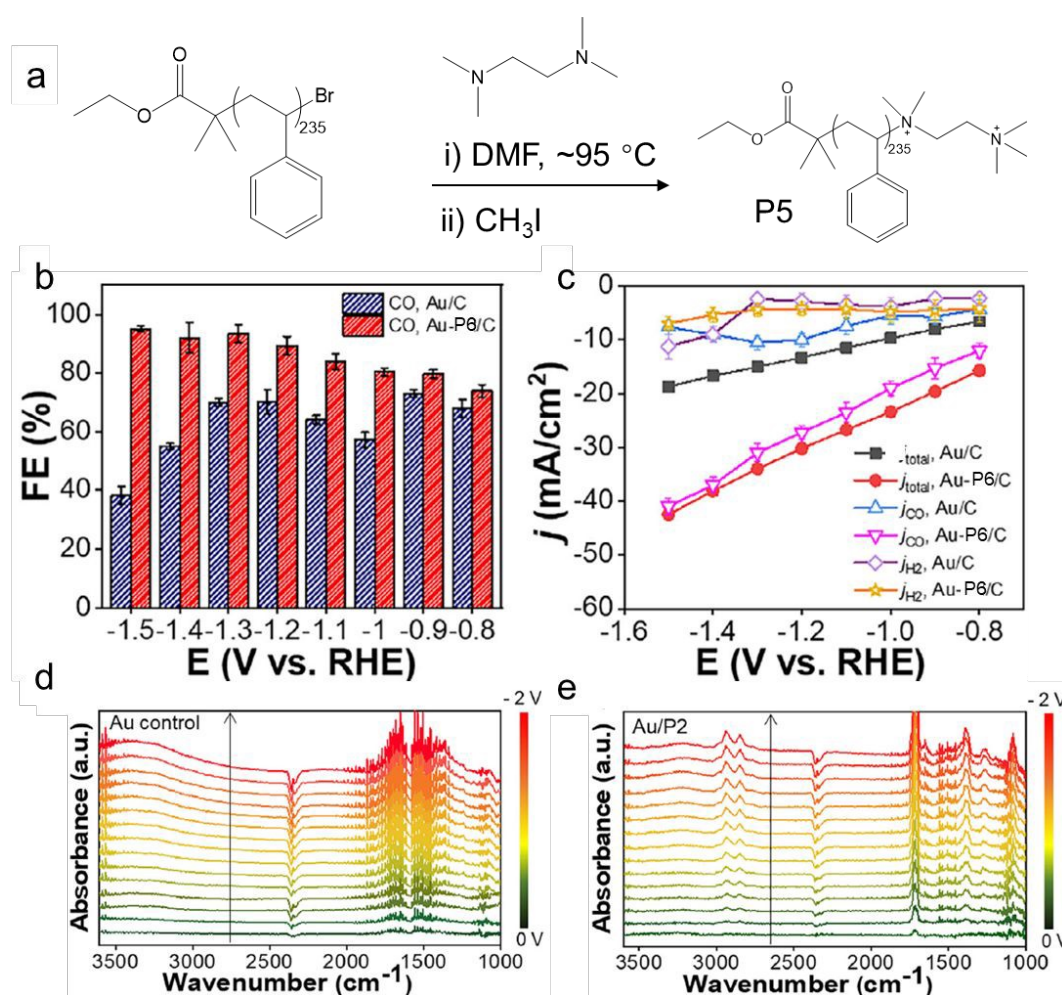


Figure 10. (a) Synthesis of quaternary ammonium-containing polymers, P5. CO FE of Au/C (b) and Au-P5/C (c) In situ ATR-SEIRAS spectra of Au control (d) and Au-P5 (e) within the range of 0 to -2 V with an interval of about -134 mV. Reproduced with permission.¹⁵³ Copyright 2025 Wiley.

ATR-SEIRAS was used to probe the change of catalyst-electrolyte interface under CO_2 reduction conditions. On Au control, spectra collected during a cathodic sweep from 0 to -2.0 V revealed a broad O–H stretching band near

3450 cm^{-1} from adsorbed water, whose intensity increased with negative bias, consistent with water dipoles aligning H-down on the negatively charged electrode (**Figure 10d**). In the presence of P5, this O–H band redshifted to 3230 cm^{-1} , about 220 cm^{-1} lower than that on bare Au (**Figure 10e**). This is consistent with hydrophobic NHC ligands where the formation of densely hydrogen-bonded water clusters is promoted by the hydrophobic microenvironment of the polymer. The peak deconvolution at –2.0 V showed that strongly H-bonded water accounted for ~92% on P5, compared with 41% on Au, suggesting that interfacial water was highly structured with strong intermolecular hydrogen bonding, thereby suppressing HER. Additional upward peaks at 2938 and 2848 cm^{-1} , corresponding to the C–H stretching of P5, became more pronounced with increasingly negative potentials, suggesting electrostatic attraction of the cationic polymer toward the electrode surface. A new peak at 1386 cm^{-1} , assigned symmetric stretching of hydrated bicarbonate, also appeared under cathodic bias, along with peaks between 1000–1200 cm^{-1} from bicarbonate hydration clusters. This peak intensity similarly increased with the negative bias, suggesting that the positively charged quaternary ammonium groups of P5 draw bicarbonate counterions toward the interface. Thus, the polymer ligands reorganized the interfacial environment by preconcentrating bicarbonate ions and structuring interfacial water, thereby enhancing CO_2 accessibility and suppressing HER, collectively improving CO_2 reduction selectivity.

Polycations with different head groups can profoundly influence the interfacial environment and product distribution in e CO_2 RR by simultaneously tuning local hydrophobicity and ion transport. Recent studies systematically examined this effect using hydrophobic para-terphenyl-trifluoroheptan-2-one copolymers (*p*TPN) functionalized with six distinct quaternary ammoniums on the side chains, including trimethylammonium (TMA $^+$), piperidinium (Pip $^+$), pyridinium (Py $^+$), 1-methyl-imidazolium (Meim $^+$), 1-n-hexyl-imidazolium (Hexim $^+$), and 1-methyl-benzimidazolium (Beim $^+$) (**Figure 11a**).¹⁵⁴ These polymer ligands were mixed with commercial CuNPs (30–50 nm) and dropped on glassy carbon as working electrode for e CO_2 RR in a H-cell with 0.1 M KHCO₃ (**Figure 11b**). The results indicated that *p*TPN-TMA $^+$ and Pip $^+$ had a high H₂ FE of ~40% and ~50%, respectively. *p*TPN-Py $^+$ enhanced the CO₂ selectivity up to ~54% at –1.2 V, while the H₂ FE is still over 40%. For *p*TPN-Meim $^+$, the H₂ selectivity was as high as 80% at –1.2 V. Increasing the hydrophobicity at N3 position (i.e., *p*TPN-Hexim $^+$), the H₂ FE decreased to ~55% at –1.2 V. For *p*TPN-Beim $^+$, the H₂ FE was significantly inhibited to ~16% and the overall C2 $^+$ product selectivity was high to 75.9% at –1.2 V (**Figure 11c–h**). Cyclic voltammetry in nonaqueous electrolytes with dissolved R₄N $^+$ cations showed that, i) reduced peak currents increased in the presence of Py $^+$, Beim $^+$ and Meim $^+$, and ii) the imidazolium cations improved CO₂ reduction kinetics as compared to Py $^+$. ATR-SEIRAS was used to gain the details of surface species during the CO₂ reduction by *p*TPN-Beim $^+$ modified Cu electrode. A vibrational peak at ~1666 cm^{-1} was assigned to the chemically bound carboxylate CO₂ $^-$ as the Beim-CO₂ $^-$ adduct, and another peak the vibration band at around 1758 cm^{-1} arose from bound *COOH, by further protonation of Beim-CO₂ $^-$. Both the linear-bonded *CO_L at 2100–1960 cm^{-1} and bridge-bonded *CO_B at ~1830 cm^{-1} were detected



on *p*TPN-Beim⁺ with a high coverage (**Figure 11i**), as compared with other ammoniums. In addition, the ratio of $\nu(\text{CO}_\text{L})$ to $\nu(\text{H}_2\text{O})$ band intensity of *p*TPN-Beim⁺ was also higher than that of *p*TPN-TMA⁺ and *p*TPN-Meim⁺ (**Figure 11j**), allowing the C–C bond coupling to C2⁺ products. Therefore, the *p*TPN-Beim⁺ improved the conversion of CO₂ to *CO and high *CO coverage by multiple (strongly) adsorbed *CO species, leading to high C2⁺ selectivity by *CO dimerization (**Figure 11k**). Meanwhile, the hydrophobicity of Beim⁺ cation disfavored the adsorption of water at the electrode-electrolyte interface.

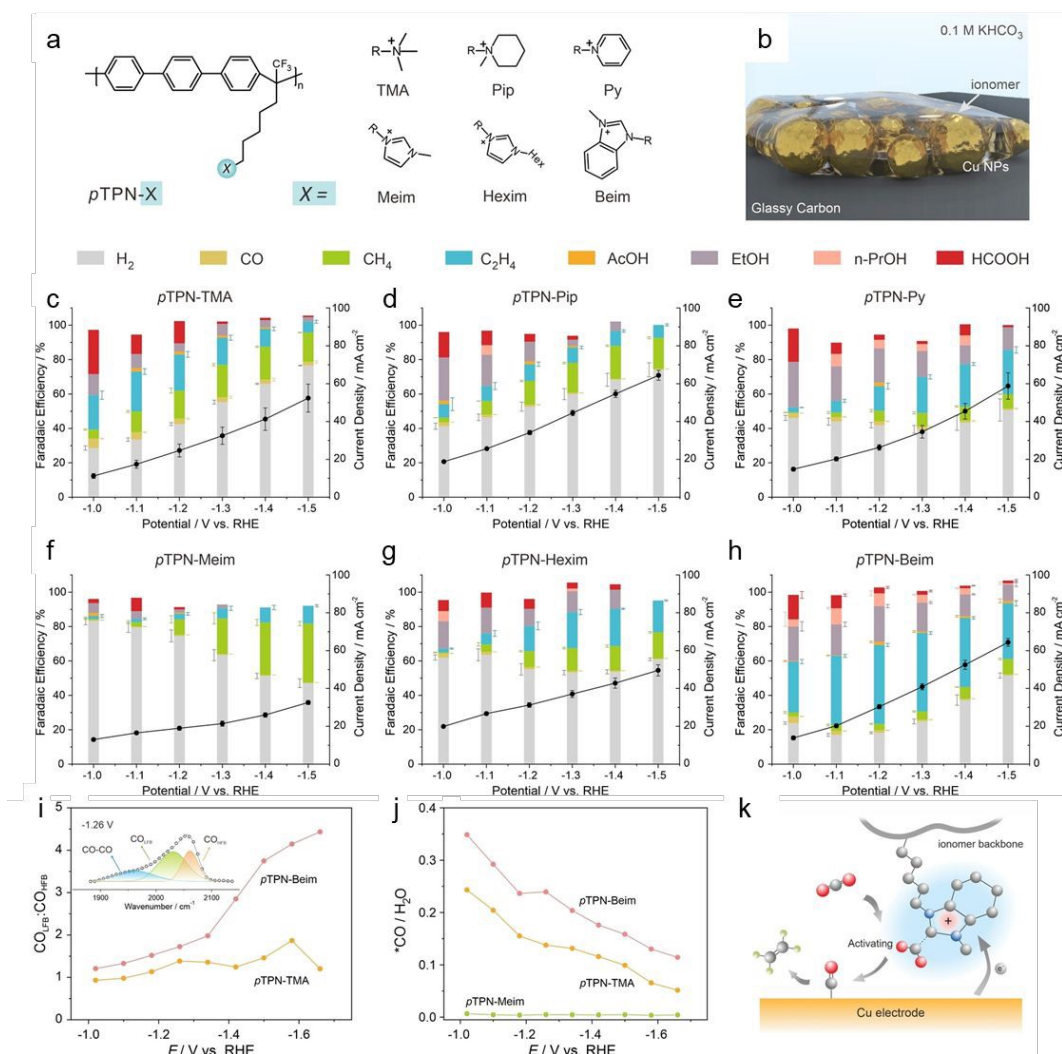


Figure 11. (a) Structural illustration of the pTPN-X ionomers. (b) Scheme of the pTPN-X-modified Cu electrode (Cu/pTPN-X) for eCO₂RR. (c–h) Products distribution and current densities over the Cu/pTPN-X electrodes. (i) Ratios of *CO_{LFB} to *CO_{HFB} band intensity against the applied potentials. Inset gives a typical peak decomposition of the ATR-SEIRAS acquired on the Cu/pTPN-Beim at -1.26 V. (j) Ratios of $\nu(\text{CO}_\text{L})$ to $\nu(\text{H}_2\text{O})$ band intensity



against the applied potentials. (k) Schematic illustration of the Beim+ cation-enhanced CO₂RR toward C₂H₄ production. Reproduced with permission.¹⁵⁴ Copyright 2023 Wiley.

The charge density of polycations also played an important role in the selectivity of eCO₂RR. Andrew's group prepared ionic polymers with quaternary ammoniums through post-functionalizing poly(pentafluorophenyl acrylate)₁₀₀ using N-boc-1,6-hexanediamine, followed by acid deprotection (PAM-1).¹⁵⁵ Ammonium-containing copolymers PAM-2 (35% methylation), PAM-3 (65% methylation) and PAM-4 (100% methylation) were prepared by methylating PAM-1 with methyl iodide. The higher ethylene FE was seen for Cu-PAM-1 with free amines and Cu-PAM-4 with 100. The pendant amine groups in PAM-1 are likely to promote ethylene formation by increasing the local basicity near the catalytic sites.

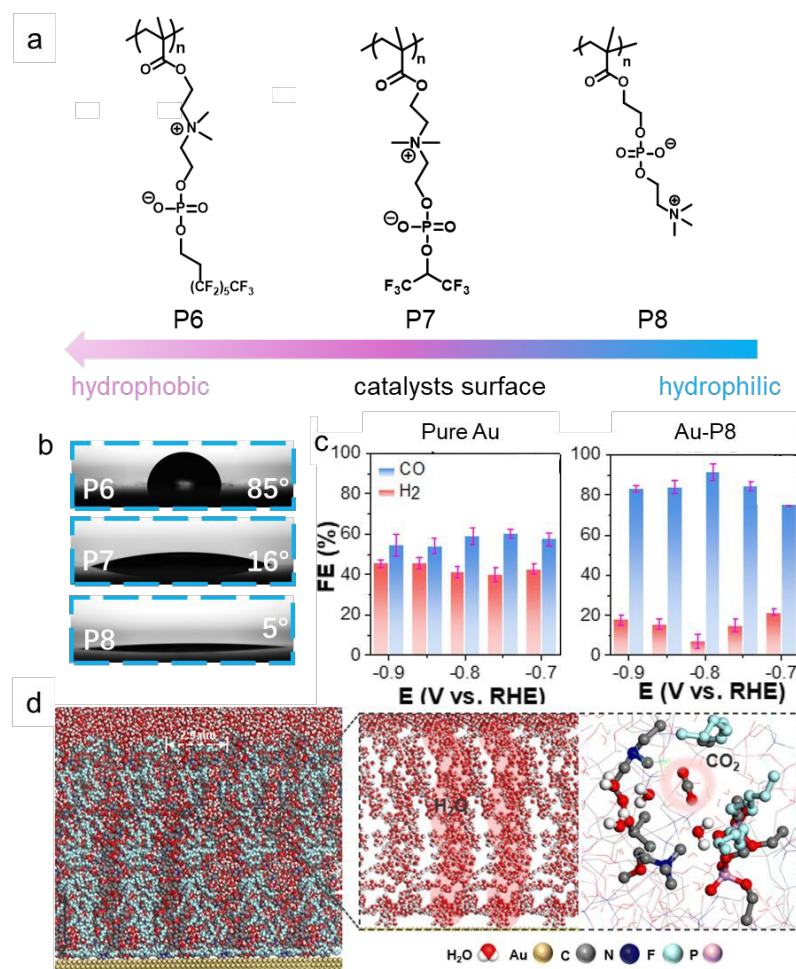


Figure 12. (a) Chemical structures of zwitterion polymers: P6-P8. (b) Water contact angles of P6-P8 coated surfaces. (c) CO and H₂ FE of Au and Au-P6. (d) MD simulation of a representative system configuration (left) and zoomed-in area of water distribution and solvated CO₂ molecule (right). Reproduced with permission.¹⁵⁶ Copyright 2024 The Royal Society of Chemistry.

To balance CO_2 and protons transport, our group reported the use of hydrophobic zwitterions, e.g., fluorinated poly(2-methacryloyloxyethyl phosphoryl choline) (polyMPC, P6) for eCO₂RR (**Figure 12a**).¹⁵⁶ Compared with P8, the catalyst surface had a WCA of 85°, indicating a nearly perfectly balanced hydrophilicity-to-hydrophobicity (**Figure 12b**). In the case of Au-P6, the J_{CO} is 3.6 times higher and $n_{\text{CO}}/n_{\text{H}_2}$ is 9 times greater than that of Au/C at -0.9 V (**Figure 12c**). The $n_{\text{CO}}/n_{\text{H}_2}$ decreased to 3.5 (Au-P6) as fluorinated content decreased, showing that fluorinated groups are important for enhancing the CO₂-to-CO selectivity. Small angle X-ray scattering (SAXS) showed that P6 comprises branched cylinders and unstacking lamellae after fitting the scattering pattern with a combined cylindrical and lamellar model with a d -spacing of 2.9 nm. MD simulation revealed that phase separation ionic and fluorinated domains in P6, providing two pathways for mass transport of water and CO₂. Water molecules penetrate extensively into the zwitterionic channels, forming continuous hydrogen-bonded chains with average hydrogen bonding density of 1.9. CO₂ preferentially associates with fluorinated tails, aligning oxygen atoms toward ammonium groups (**Figure 12d**). This phase-separated microstructure improves mass transfer kinetics and enhances CO₂ reduction efficiency, achieving a 50–80% increase in FE and suppressing HER.

Ionic polymers, depending on the content of ionic groups, are not stable in an aqueous solution. To prevent swelling, or potential dissolution during electrolysis, cross-linking may be essential to enhance mechanical robustness and chemical resistance. The cross-linked polyelectrolyte, while providing similar ionic transport control, forms a robust and stable interfacial layer that effectively immobilizes catalysts. Gu *et al.* used 1,6-diiodohexane to cross-link the copolymer of diallyldimethylammonium chloride and diallylmethylamine and obtained cross-linked polyelectrolyte layer (c-PDDA) on the surface of metal catalysts.¹⁵⁷ Using AgNPs and InNPs as the model catalysts, they studied the eCO₂RR performance under acidic conditions. c-PDDA coated AgNPs had the highest CO FE of 95 ± 3% at -1.57 V vs. standard hydrogen electrode (SHE) at the current density of -100 mA cm⁻². The coated AgNPs were stable and maintained the CO FE of > 80% for electroreduction over 36 h at -200 mA cm⁻², while CO FE of bare AgNPs decreased 52% after 10 h (43%) (**Figure 13a, b**). For c-PDDA coated InNPs, the highest FE of formate was 76 ± 3% at -1.84 V vs. SHE at the current density of -200 mA cm⁻². Both uncoated AgNPs and InNPs primarily produce H₂, due to the high proton concentration in 0.1 M H₂SO₄ electrolyte (**Figure 13c, d**).



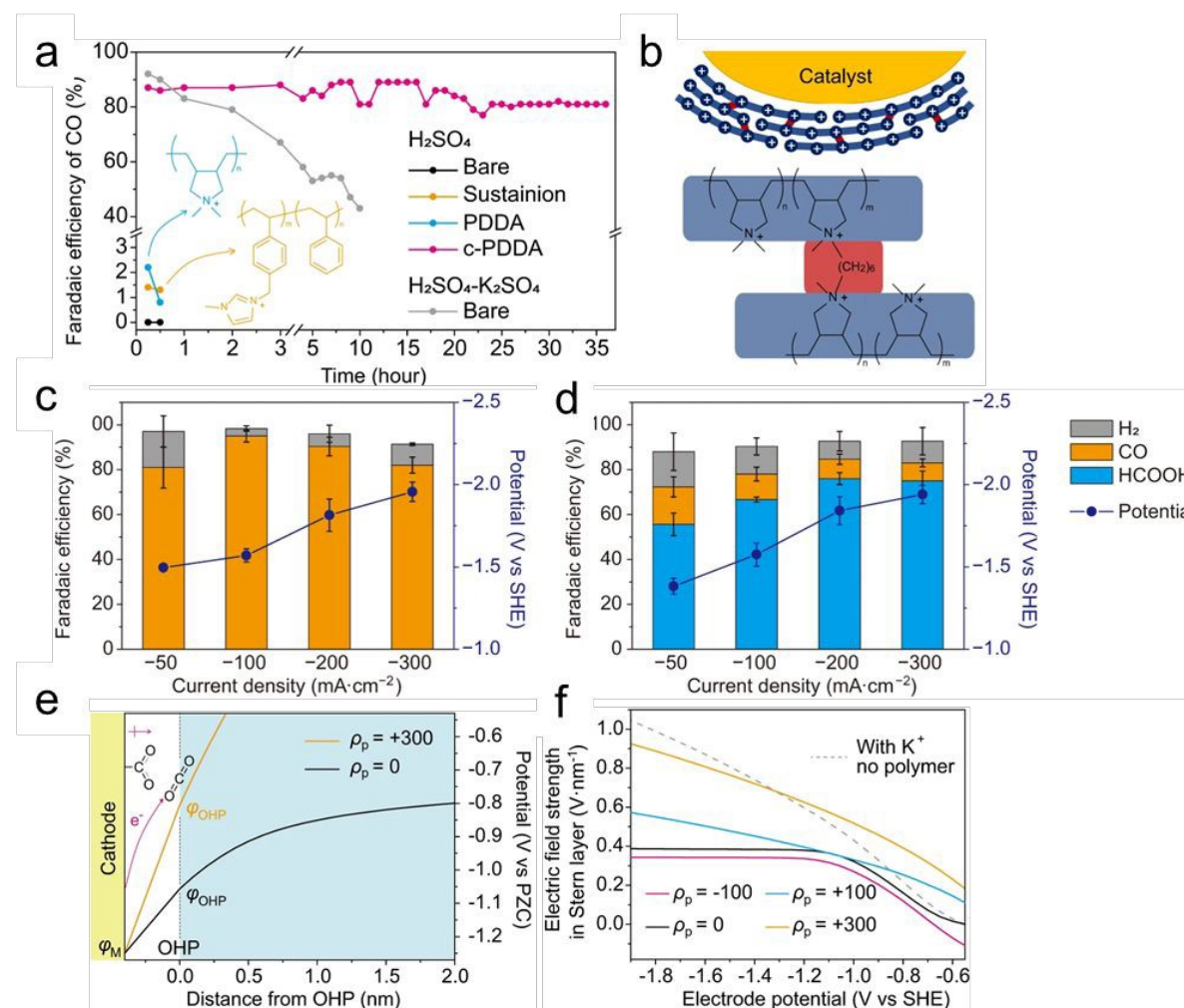


Figure 13. (a) CO FE during electrolysis with a constant current density of -200 mA cm^{-2} . Bare Ag NPs (black), Sustainion XA-9 modified Ag NPs (orange), PDDA modified Ag NPs (blue) and c-PDDA modified Ag NPs (magenta). (b) Schematic of c-PDDA modified catalyst. (c, d) H₂ FE (gray), CO FE (orange) and formic acid (blue), and the electrode potential (dark blue curves), while (c) Ag NPs and (d) In NPs were used as the catalysts. (e) Potential profiles on Ag electrodes covered by polymer layers with $\rho_p = 300 \text{ C cm}^{-3}$ (orange curve) and $\rho_p = 0$ (black curve) in 10 mM HOTf at -1.8 V vs. SHE. Schematic of the rate determining step of CO₂ reduction is shown. (f) Plots of the electric field strength in Stern layer based on the electrode potential. Solid curves: Ag electrodes covered by polymer layers with different ρ_p (unit: C cm^{-3}) in 10 mM HOTf. Gray dashed curve: Bare Ag electrode in 10 mM HOTf + 40 mM KOTf. Reproduced with permission.¹⁵⁷ Copyright 2023 Springer Nature.

To understand the underlying mechanism, the different polymers coated Ag micro-disk electrode (MDE) and the simulation of generalized modified Poisson-Nernst-Planck (GMPNP) modeling were conducted. The HER polarization curves of Ag MDEs coated by c-PDDA, Sustainion XA-9, PTFE and Nafion D520, were collected in 10 mM of trifluoromethanesulfonic acid (HOTf). When coated by neutral PTFE, the plateau region is lower than

pure Ag MDE, indicating the limited diffusion coefficient of H^+ in PTFE. For cationic c-PDDA and Sustainion XA-9 coated Ag MDE, the plateau current is lower than that of PTFE coated Ag. In particular, the c-PDDA coated Ag MDE had the lowest limiting current. The positively charged polymers therefore showed a suppression of the mass transport of H^+ . Since the cation density of c-PDDA was 3 times that of Sustainion XA-9, the c-PDDA coating acted as the best layer to stop the diffusion of proton. The GMPNP results indicated that the migration rate of H^+ decreases with the increase of total charge density (ρ_p) of immobilized ionic sites (positively charged c-PDDA) and movable ions (cations). In addition, the c-PDDA also changed the local pH near the cathode and the electric field strength in Stern layer (E_{stern}). For c-PDDA, H^+ reduction can increase the local pH at outer Helmholtz plane (OHP). Meanwhile, the CO_2 reduction generates OH^- that neutralizes H^+ and further increase of local pH. For CO_2 reduction to CO , the single-electron reduction of CO_2 ($CO_2 + e^- \rightarrow CO_2^-$) is the rate determining step (RDS). As shown in **Figure 13e**, the driving force of electron transfer from cathode to CO_2 was from potential difference between cathode and OHP. With a higher E_{stern} in the presence of positively charged c-PDDA, the CO_2 reduction became favorable (**Figure 13f**).

Cross-linked poly(ionic liquid) (PIL) coated metal catalysts can be obtained through in situ polymerization of ionic liquid monomers. For example, Xu *et al.* prepared the poly(imidazolium-pyridine-imidazolium) coated CuNPs by adding CuNPs into imidazolium-pyridine-imidazolium, the PIL layer was formed by in situ radical polymerization and cross-linked by divinylbenzene (**Figure 14a**).¹⁵⁸ The effect of counter ions on e CO_2 RR performance was investigated in a flow cell that equipped with gas diffusion electrode (GDE) and anion exchange membrane (AEM). For CuNPs coated by PIL with F^- counter ions (Cu@PIL-F), the H_2 FE, CO FE, HCOO- FE were 7.9%, 67.9% and 12.6% respectively. However, the H_2 FE of Cu@PIL with PF_6^- counter ions was 72.0%. The H_2 FE increased with the order of F^- (12.2 %) < Cl^- (14.9 %) < Br^- (24.4 %) < I^- (39.9 %) < BF_4^- (47.6 %) < PF_6^- (72.0 %) (**Figure 14b**). The LSV curves indicate that Cu@PIL-F exhibits high catalytic activity for both HER and e CO_2 RR, with the e CO_2 RR activity surpassing that of HER, leading to a low H_2 FE. The CO_2 -temperature programmed desorption (TPD) showed the intense chemisorption peaks at over 300 °C and a broad strong physisorption bond at ~158 °C for Cu@PIL-F, indicating the enriched local CO_2 concentration at the interface, thereby improving its mass transport. The highest occupied molecular orbital (E_{HOMO}) of F^- was 2.103 eV and the number of electrons transferred from F^- to cation was 0.756; whereas, those of PF_6^- were -5.301 eV and 0.248. Therefore, F^- as counter ions was considered to have higher electron-donating ability that facilitates e CO_2 RR, compared to other counter ions (**Figure 14c**). In addition, imidazolium-containing PIL also enriched the local concentration of CO_2 through the formation of CO_2 adducts. Cu@PIL-Cu₂O hybrid catalysts with Cu₂O was deposited on the surface of PIL shell on Cu exhibited a high FE (C2+) of 76.1% at -0.85 V.¹⁵⁹



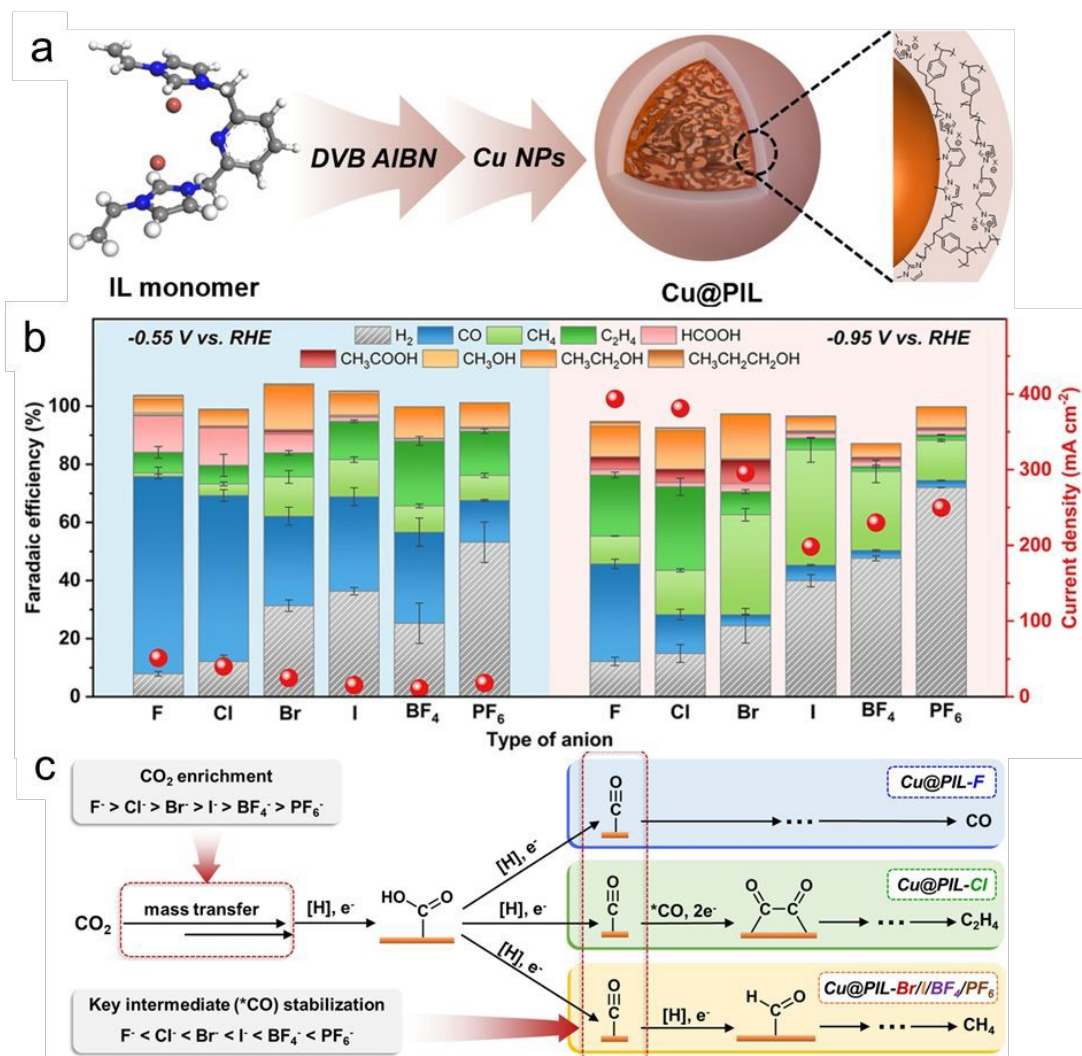


Figure 14. (a) Schematic illustration for the structure of IL monomer and the preparation of Cu@PIL. (b) eCO₂RR performance of Cu@PIL-X-1.2 with different anions (light blue area (left): at the cathodic potential of -0.55 V; light red area (right): at the cathodic potential of -0.95 V). (c) Proposed pathway of Cu@PIL catalyzed eCO₂RR with different anions. Reproduced with permission.¹⁵⁸ Copyright 2021 Elsevier.

6. Porous polymer coated nanocatalysts for eCO₂RR

Metal–organic frameworks (MOFs) and covalent organic frameworks (COFs), both of which have unique porous and crystalline architectures, have also emerged as highly promising materials for the electrochemical reduction of eCO₂RR.^{160–163} MOFs consist of metal ions or clusters coordinated with organic linkers, while COFs, in contrast, possess covalently linked, π -conjugated backbones rich in heteroatoms (e.g., N, S).^{164–166} The periodic three-dimensional networks with ultrahigh surface areas ($>1,000$ m² g⁻¹) and tunable pore sizes can enable efficient CO₂ adsorption/storage and control the mass transport of CO₂/intermediate, potentially promoting deep reduction of CO₂.^{167, 168} The presence of catalytically active metal centers or single-atom sites within porous frameworks allows

fine control over the binding energies and stabilization of, providing structural robustness and facilitating charge transport.¹⁶⁹⁻¹⁷³ Moreover, their tunable pore microenvironments allow precise control of local reaction conditions, such as electrode–electrolyte interactions and solvent effects, effectively enabling selective formation of CO₂ reduction products.¹⁷⁴⁻¹⁷⁶

To directly evaluate the impact of well-defined porous structures on tuning the local environment around the active sites, one can grow catalytically non-active MOFs on a catalytic active metal electrode. For example, Hod's group coated a thin layer of Zr₆-oxo based MOF (UiO-66) with a control thickness in the range of 0.5 to 1.8 μm on an Ag foil.¹⁷⁷ Compared to pure foil, Ag coated with ~0.9 μm of UiO-66 showed 43% increase in CO selectivity at -0.8 V. The enhancement was attributed to abundant defect sites in UiO-66, characterized as the Brønsted acid, Zr-OH. These acid sites promote CO₂ reduction by acting as the proton sources which can stabilize the activated *COO⁻ intermediates. To verify this mechanism, the adsorption and desorption of OH⁻ as a probe was studied. The results indicated that overpotential required for OH⁻ absorption on UiO-66 coated electrodes was lower than on pure Ag electrode. Using benzoic acid to cap the OH sites on MOF surfaces, the CO FE of modified Ag-UiO-66 dropped by 21%. Similarly, they studied the impact of the nitrile-functionalized UiO-66 (or UiO-66-CN) on a Bi electrode. Compared with pure Bi, the UiO-66-CN coating achieved an FE of HCOOH up to 93% and exhibited 7 times faster kinetics, due to the porous MOF acting as a CO₂ reservoir. Because of the high concentration of BA-CN groups, the local CO₂ concentration near the Bi catalyst increased to ~0.82 M, which was ~ 27-fold higher than that in the bulk electrolyte (~0.030 M), as indirectly calculated from the ATR-IRRAS at different CO₂ concentrations. In addition, the value was confirmed using quinone as a redox probe which reversibly binds with CO₂.¹⁷⁸

To prepare MOF-NP or COF-NP composites, various synthetic strategies have been developed and recently summarized in review papers.¹⁷⁹⁻¹⁸³ In general, there are two straightforward methods. The first method is the “impregnation” where a MOF or COF powder is mixed with a solution containing metal precursors (or mixing them in the solid state), followed by the reduction inside (mostly) or on the external surface of the MOF or COF. The second is in situ growth of MOF or COF on pre-synthesized NPs, leading to the encapsulation of NPs within the framework. In the latter case, embedding pre-synthesized NPs avoids disrupting a single lattice plane, whereas impregnation involves lattice distortion during NP growth.

Cu₂O@MOF on Cu foil (Cu₂O@MOF-CF) was prepared by heating the mixture of CuSO₄·5H₂O, 1,3,5-tris(1-imidazolyl)benzene and 4,4'-biphenyldicarboxylic acid with NaOH activated Cu foil.¹⁸⁴ The C₂H₄ FE of Cu₂O@MOF-CF was 48.6% at -1.11 V, about 2.2 times of that for pure Cu foil. The enhanced ethylene selectivity was attributed to the surface Cu₂O, which generated more *CO intermediate, leading to a high *CO coverage on the Cu foil and facilitating C–C coupling of C₂H₄. As confirmed by DFT calculation, the Cu₂O@MOF showed a



lower free energy of first electron transfer step and weaker CO adsorption energy. $\text{Cu}_2\text{O}@\text{MOF-CF}$ also exhibited 70 times greater surface area, compared to pure Cu foil, indicating that porous $\text{Cu}_2\text{O}@\text{MOF}$ provided more active sites for CO_2 activation. In a more recent study, $\text{Cu}@\text{MOF}$ prepared on the Cu foil through microwave synthesis was reported with higher selectivity to C_2H_4 by Zhang *et al.*¹⁸⁵ Interestingly, $\text{Cu}@\text{MOF}$ converted to Cu nanocubes during electrolysis, and its FE to C_2H_4 was 49.6%, much higher than that of Cu foil (~25% of C_2H_4 FE). The coating of MOF on catalytic metal also provided the local electric field that improved the adsorption energy of *CO. The growth of oriented NiCu-MOF nanorod array on Cu_2O ($\text{Cu}_2\text{O}@\text{MOF/CF}$) via solvothermal synthesis improved the ethanol selectivity, 44.3% at -0.615 V.¹⁸⁶ DFT calculations indicated that an internal electric field polarization between Cu_2O and NiCu-MOF, resulting from the asymmetric electron distribution, enhanced the adsorption of *CO and enabled the C–C coupling. Similarly, atomically dispersed Co^{2+} in COF by mixing CoCl_2 with redox-active COF, achieving ~66.8% FE ethanol at -2.87 mA cm^{-2} .¹⁸⁷ The reversible variation in oxidation state of Co^{2+} endow catalyst with high stability. The ~20% of current loss is observed, and FE ethanol remains ~60% after electrolysis at -0.67 V over 24 h.

A more structurally conservative yet highly effective strategy to enhance the catalytic performance of MOFs is the incorporation of strong coordinating ligands into their frameworks. This approach preserves the intrinsic crystallinity and porosity of the MOF while introducing well-defined coordination environments capable of stabilizing active metal centers. After the formation of the MOF skeleton, catalytic metal ions or nanoclusters can be precisely encapsulated through coordination interactions, enabling atomic-level control over the geometry and electronic structure of active sites. Chen *et al.* demonstrated the synthesis of Cu-containing Zr-based UiO-67 by incorporating a NHC precursor, dibenzyl imidazolium, during solvothermal synthesis of MOF. Afterwards, CuCl_2 was introduced under alkaline conditions, NHC-Cu was produced within the pores as $2\text{Bn-Cu}@\text{UiO-67}$ (**Figure 15a**).¹⁸⁸ The CH_4 FE of $2\text{Bn-Cu}@\text{UiO-67}$ reached 81% at -1.4 V. DFT simulation suggested that the charge transfer from NHC to the Cu stabilized *CO on the Cu site, promoting further hydrogenation. This was aligned with infrared spectroscopy studies on the formation of *OCH₃ at 1110 cm⁻¹ with $2\text{Bn-Cu}@\text{UiO-67}$. Similarly, the imidazolium carboxylate functionalized NHC-based COF (NHC-CO₂-COF) was demonstrated to prepare metal-NHC@COF under mild conditions.¹⁸⁹



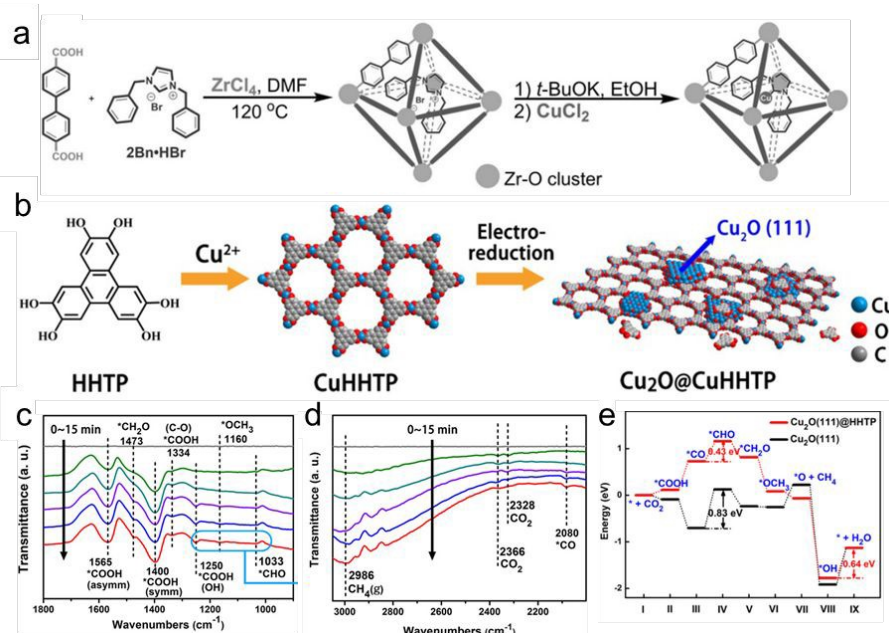


Figure 15. (a) Synthetic scheme of 2Bn-Cu@UiO-67. Reproduced with permission.¹⁸⁸ Copyright 2021 Wiley. (b) Solvothermal synthesis of CuHHTP and preparation of Cu₂O@CuHHTP via electrochemical treatment of CuHHTP at -1.2 V for 30 min. (c-e) Operando ATR-FTIR spectra on Cu₂O@CuHHTP collected at -1.4 V vs. RHE in CO₂ saturated 0.1M KCl/0.1M KHCO₃ electrolyte. (h) Proposed mechanism of Cu₂O@CuHHTP for the formation of CH₄. (i) Free-energy diagrams of eCO₂RR to CH₄ for Cu₂O-(111)@HHTP (red line) and pristine Cu₂O(111) crystal plane (black line). Reproduced with permission.¹⁹⁰ Copyright 2020 Wiley.

Cu₂O-MOF hybrid catalysts provide an excellent example of how MOF-based systems can tune product selectivity. CH₄ is thermodynamically favored on Cu due to its low reduction barrier (-0.24 V at pH 7). However, high CH₄ selectivity faces a kinetic disadvantage because of eight-electron transfer and the formation of multiple products from different facets of the nanocatalysts. On a conductive copper-based MOF (CuHHTP), Cu₂O could be synthesized through in situ electroreduction. After 30 minutes of electroreduction, Cu₂O NPs with an average size of ca. 3.5 nm grow uniformly on CuHHTP, where periodically distributed CuO₄ nodes would be expected (Figure 15b).¹⁹⁰ Cu₂O when supported on conductive carbon black (Cu₂O@CCB) and commercial Cu₂O showed a CH₄ FE of 30% and 15%, respectively. Cu₂O@CuHHTP was highly selective to CH₄ with a FE of 73% FE at -1.4 V owing to the highly exposed Cu₂O (111) single lattice plane. ATR-FTIR showed the peaks corresponding to key intermediates for CO₂ hydrogenation: 1250 cm⁻¹, 1334 cm⁻¹, 1400 cm⁻¹, 1565 cm⁻¹, assigning to the OH deformation, C-O stretch, symmetric stretch, and asymmetric stretch of *COOH intermediate, respectively (Figure 15c). Meanwhile, the peak at 2080 cm⁻¹, corresponding to *CO intermediate, was blue shifted relative to reported value (~2065 cm⁻¹), probably due to the hydrogen bonding between *CO and hydroxyl group of HHTP (Figure 15d). DFT simulation indicated that CO₂ was absorbed on Cu₂O (111) and converted to *COOH, and all key

intermediates, e.g., $^*\text{CHO}$, $^*\text{CH}_2\text{O}$ and $^*\text{OCH}_3$, were stabilized by hydrogen bonding with HHTP. The free energy diagram (**Figure 15e**) highlighted in the key transition step from $^*\text{CO}$ to $^*\text{CHO}$ where the free energy barrier decreases from 0.83 eV to 0.43 eV in the presence of HHTP. Similarly, Cu@THQ consisting of tetrahydroxy-1,4-quinone (THQ) with square-planar CuO_4 nodes had similar 2-D conductive network. Up on reduction, the formation of metallic Cu (5.5 nm) instead of Cu_2O was selective to C_2H_4 with an FE of 42%.¹⁹¹

The MOF framework also influenced the formation of NPs during the reduction of metal precursors via impregnation. For example, Hwang's group studied the formation of Pd and AuPd bimetallic NPs through in situ (co)reduction of $\text{Pd}(\text{NO}_3)_2$ and HAuCl_4 within Zr-MOF-808.¹⁹² Under significant local tensile strain provided by the MOF skeletons, the lattice expansion of Pd (with or without Au) showed was as large as $\sim 2.6\%$, compared to those of the Pd/C. This tensile strain had a pronounced influence on catalytic behavior by weakening the adsorption of $^*\text{CO}$ species. The eCO₂RR efficiency of Pd and AuPd bimetallic NPs was significantly higher than that of Pd/C. The FE to formate for MOF-Pd and MOF-AuPd was 90% and 99%, respectively.

COFs, on the other hand, often have extended π -conjugated skeletons and abundant N sites to promote electron delocalization, particularly attractive as the catalyst support for eCO₂RR.^{193, 194} The COF prepared from 2,3,9,10,16,17,23,24-octahydroxyphthalocyaninato copper (CuPc-8OH) could support the growth of Cu nanoclusters (Cu-NC@CuPc-COF) through impregnation of Cu^{2+} and in situ reduction with hydrazine.¹⁹⁵ The nanoconfinement provided by the nanochannels in the COFs limited the overgrowth of Cu, resulting in Cu nanoclusters with 1.2 nm. The conductivity of Cu-NC@CuPc-COF contributed largely to its high partial current density, *i.e.*, 538 mA cm⁻² at -1.2 V with CH_4 FE up to 60%. A unique advantage of COFs lies in their ability to mediate ion transport through cation- π interactions. Such interaction can guide ion accumulation along specific channels and change the local availability of protons/hydroxides. A recent study by Ozden *et al.* demonstrated this concept by constructing a bulk heterojunction on catalysts by coating hydrophobic Hex-Aza-COF on CuNPs. The resulting hybrid achieved a remarkable energy efficiency (EE) towards C_2+ of 18% at J_{C_2+} of 127 mA cm⁻².¹⁹⁶ In a membrane electrode assembly (MEA) electrolyzer, the accumulation of cation (K^+) on the surface of cathode can significantly limit the CO adsorption and consequently promotes HER. With COF coating, the diffusion of K^+ was slowed down by three-order of magnitude. DFT calculations indicate that the hydrophobic COFs constrict K^+ migration while enhance OH^- adsorption, facilitating C-C coupling. Similarly, Shao and co-workers demonstrated that Cu single atoms or nanoclusters grown in the COF made of 2,6-diaminoanthraquinone(DAAQ) and 2,4,6-triformylphloroglucinol (TFP) were selectivity for eCO₂RR to CH_4 .¹⁹⁷ Cu nanoclusters in DAAQ-TFP-COF had an FE of CH_4 about 56% at -1.26 V. The DFT results suggested that the C=O groups of DAAQ-TFP coordinated with K^+ cations, which largely suppressed the surface adsorption of water. Similarly, Cao *et al.* encapsulated Cu nanocluster into NiPc-COF by dispersing Cu_{32} cluster on NiPc-COF, where Cu promotes C-C coupling while porous



COF provides high CO_2 adsorption of $16.8 \text{ cm}^3 \text{ g}^{-1}$.¹⁹⁸ The FE($\text{C}2+$) of 57.1% was achieved with a current density of 353.3 mA cm^{-2} at -1.6 V . In addition to Cu nanoclusters, other metal clusters and single-atom catalysts have been shown to exploit COF channel confinement to regulate mass transport and electronic structure, thereby enhancing e CO_2 RR efficiency.¹⁹⁹⁻²⁰¹

COF ionomers, prepared by chemically linking building blocks containing multiple ionic groups^{202, 203 204, 205}, can benefit from both the porosity and local electric field. For example, a catalyst ink was prepared by physically mixing commercial CuNPs with a sulfonated 2D COF ionic nanosheet (NUS9).²⁰³ The porous COF backbone with a high density of ionic groups enhanced the local concentration of CO_2 and K^+ , promoted the dissociation of H_2O , mitigated the $^*\text{CO}$ coverage on the catalyst surface, and lowered the rate determining step (RDS) for CH_4 production (i.e., $^*\text{CO} + ^*\text{H} \rightarrow ^*\text{CHO}$). A prominent FE CH_4 of 66% in an acid electrolyte (0.5 M K_2SO_4 , pH = 2) was obtained. Meanwhile, the operation time exceeded 9 h under 200 mA cm^{-2} . In another example reported by Guo *et al.*, a quaternary ammonium salt ($\text{N}(\text{CH}_3)_4\text{Br}$) was loaded into hydrophobic COF (Me-COF) pre-modified by fluorine.²⁰⁴ Due to the strong affinity between quaternary ammonium cations and bicarbonate, Me-COF showed a high CO_2 adsorption capacity than bare COF. The C_2H_4 FE increased from $\sim 18\%$ to 36% at 200 mA cm^{-2} after modifying Cu electrode by Me-COF. In practical alkaline zero-gap MEA devices, the C_2H_4 FE reached 46.6% at 500 mA cm^{-2} with a cell voltage of 3.61 V. The *in situ* ATR-SEIRAS and Raman suggested that Cu/Me-COF had a higher surface coverage with $^*\text{CO}$ intermediate and favored $^*\text{CO}$ dimerization. The $v(^*\text{CO}_\text{L})/v(\text{H}_2\text{O})$ area ratio for the Cu/Me-COF electrode was noticeably higher than pure Cu. The $^*\text{CO}$ adsorption energies from DFT on Cu (100) and Cu (100)/Me-COF were calculated to be -1.12 eV and -1.33 eV , respectively, indicating stronger $^*\text{CO}$ adsorption on the Cu (100)/Me-COF electrode.

The key challenge in using MOF-NP or COF-NP composites for e CO_2 RR is their intrinsically poor conductivity. Most MOFs are constructed from metal nodes bridged by organic linkers (non-conductive), which, although structurally crystalline and porous, typically provide limited electron conductivity. As a result, when MOF-NP composites are coated onto an electrode surface, only a small fraction of the embedded catalytic metal sites is electrochemically accessible, while the majority remain electronically isolated within the insulating MOF matrix. One solution is to convert the organic framework to carbon through calcination. Such MOF-derived composites then became NPs encapsulated in a conductive carbon network. This sacrifices the structural periodicity of MOFs, but those hybrid catalysts have proven to be extremely active in e CO_2 RR.²⁰⁶⁻²¹⁰ For example, Sun *et al.* synthesized carbon encapsulated copper-doped cerium oxide composite (Cu/CeO₂@C) by one-pot pyrolysis of MOF precursors (**Figure 16a**).²¹¹ In a flow cell, Cu/CeO₂@C had a selectivity to CH_4 of 80.3% at -1.5 V while that of Cu/CeO₂ of 59.2% (**Figure 16b**). Carbon played an important role in enhancing the conductivity of Cu/CeO₂ and promoting electron transfer. The Cu/CeO₂@C had a lower charge-transfer reactance (R_{ct}) of $\sim 9 \Omega$ measured from Nyquist



plots, as compared to Cu/CeO₂ ($\sim 14 \Omega$) (**Figure 16c**), indicating higher charge transfer and kinetics. In addition, Cu/CeO₂@C showed higher CH₄ partial current density (J_{CH_4} , 138.6 mA cm⁻²) than that of Cu/CeO₂ (J_{CH_4} , 81.5 mA cm⁻²) at -1.5 V. Similarly, HKUST-1 embedded paddle-wheel Cu dimer by pyrolysis had a C₂H₄ FE of 45% at -1.5 V.²¹²

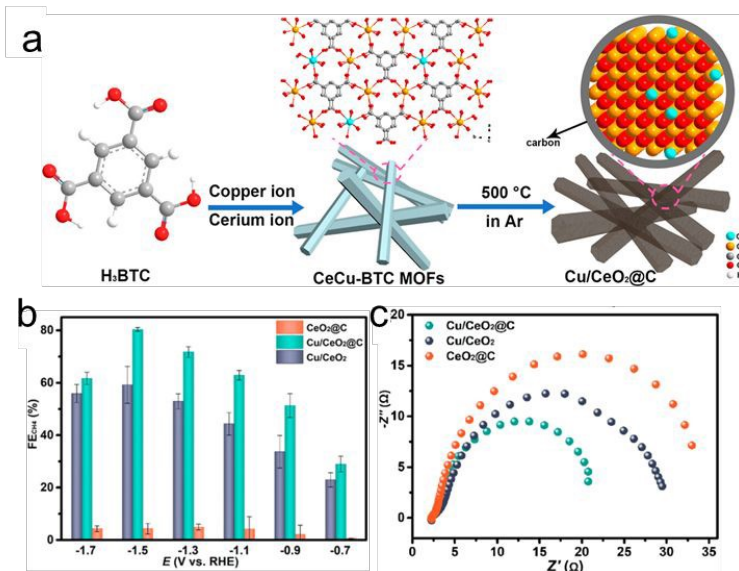


Figure 16. (a) Schematic illustration for the Synthesis of Cu/CeO₂@C. (b) Products FE of Cu/CeO₂@C at varied applied potentials. (b) The comparison of CH₄ selectivity. (c) Nyquist plots of Cu/CeO₂@C, Cu/CeO₂ and CeO₂@C. Reproduced with permission.²¹¹ Copyright 2023 American Chemical Society.

Alternatively, if metal NPs are interconnected to form a conductive network, it would allow the efficient delivery of electron for electroreduction. As demonstrated by Peng *et al.*,²¹³ PCN-222(Cu) MOF prepared from tetrakis(4-carboxyphenyl)porphyrin Cu was first impregnated with chloroauric acid that further was reduced under basic conditions. Au nanoneedles (AuNN) with an average diameter of 10 nm were formed in alignment with the MOF pore channels. AuNN@PCN-222(Cu) had a high FE of 52.5% to C₂H₄ FE at -1.2 V. As a control, scattered AuNPs formed within PCN-222(Cu) (AuNP@PCN-222(Cu)) obtained by chemical reduction under neutral conditions exhibited only ~25% of C₂H₄ FE at -1.2 V. In situ ATR-SEIRAS of AuNN@PCN-222(Cu) suggested a decreased peak at 2108 cm⁻¹ and an increased peak at 1750 cm⁻¹ as the increase of potentials, assigned to *CO adsorbed on AuNN and *CHO intermediates adsorbed on the metalloporphyrins. The DFT calculations suggest the reaction mechanism likely via a tandem pathway: CO is first generated on the impregnated Au nanoneedles, and these CO species subsequently coupled with *CHO intermediates adsorbed on the metalloporphyrins to produce C₂H₄.



7. Summary and outlook

In this review, we have summarized recent advances in nanocatalysts modified with polymer ligands for eCO₂RR, encompassing hydrophobic, conductive, ionic, and porous polymer systems. The highlighted studies collectively reveal emerging insights into how ligand chemistry governs catalytic behavior at the catalyst-electrolyte interface, potentially offering a molecular-level understanding of how interfacial engineering can enhance reactivity. The key enhancement mechanisms center around microenvironmental control, e.g., solvation structure, local CO₂ concentration, electronic structures and mass transport of ions/water, all of which create more favorable conditions for CO₂ activation and intermediate stabilization. These findings can power the next-generation design of ligands as a strategic tool to accelerate the discovery of new catalysts in eCO₂RR systems. Despite these advances, significant challenges remain in achieving precise control over polymer–catalyst interactions, dynamic interfacial behavior, and real-time characterization under operando conditions. In particular, the inherently dynamic nature of polymer–metal interfaces under bias presents fundamental challenges for establishing clear structure–function relationships in eCO₂RR.

First of all, selective surface modification of metal nanocatalysts has been overlooked currently. The reactivity of nanocatalysts is intrinsically governed by their surface energy and atomic arrangement, as determined by the exposed crystal facets. For example, CH₄ formation is favored on Cu (111) facets, whereas C₂H₄ formation occurs on Cu (100) facets.²¹⁴ The CO generation rate is 20 times higher when Pb is deposited on the Au (211) than on Au (100).²¹⁵ Hence, selectively adding polymer ligands to specific facets of nanocatalysts is a viable strategy to enhance product selectivity and reaction rate. By designing polymers with tailored functional groups or competitive ligands,²¹⁶ it becomes possible to selectively adsorb onto specific crystal planes. Ultimately, facet-selective polymer modification allows for “on demand” opening of the surface for catalysts, providing new pathways for rational design of nanocatalysts in eCO₂RR.

Second, new ligand chemistry is underdeveloped. While strong coordination between ligands and metal surfaces is generally desirable, we and others have shown that even ligands with robust coordination motifs, e.g., NHCs, underwent partial desorption under reductive potentials.^{111, 217} For example, NHCs bound to Au exhibit excellent stability within moderate potential windows, yet their electrochemical stability typically breaks down below approximately -0.8 V.²¹⁷ This limitation is acceptable for noble metal catalysts like Au and Ag but insufficient for less active Cu-based catalysts, which commonly operate below -1.0 V during eCO₂RR. Pursuing ever-stronger covalent coordination alone may not fully resolve the trade-off between stability and accessibility of catalytic sites. Instead, a promising direction is the development of polymer ligands capable of dynamic exchange on the surface, allowing reversible desorption and adsorption under electrolysis.²¹⁸ This dynamic exchange also provides the possibility to construct polymer–metal interfaces that combine long-term structural robustness. Meanwhile, ligand



desorption, chemical degradation (on the extended polymer chains, not limited to the binding motifs), and mechanical reorganization during extended electrolysis remain largely unexplored, highlighting the need for systematic studies on polymer durability and aging under realistic eCO₂RR operating conditions.

Third, most polymer ligands are catalytically inert, serving primarily as non-catalytic stabilizers rather than as active components in eCO₂RR. Introducing catalytically active motifs into polymer backbones possibly offers an emerging strategy to bridge molecular catalysis and nanocatalysis. Organic amines or ammonium groups, such as pyridine²¹⁹,²²⁰ and imidazolium derivatives,²²¹ have been shown to act as metal-free CO₂ reduction catalysts through reversible dearomatization/aromatization cycles. By incorporating these functional moieties into polymer frameworks, it becomes possible to construct hybrid catalytic interfaces where both the polymer and metal centers cooperatively participate in CO₂ activation.^{222, 223} The organic functional groups can serve as co-catalytic sites, pre-activating or even capturing CO₂.²²⁴ More rational design of redox-active and catalytically functional polymer ligands will bring the promise of cascade to couple CO₂ direct air capture and reduction.

Lastly, the development and application of advanced *in situ* characterization tools are crucial for elucidating the role of polymer ligands in eCO₂RR. At present, techniques such as ATR-SEIRAS, and *in situ* Raman as spectroelectrochemistry tools provide valuable insights into the electronic structure and the evolution of surface species. However, these methods do not fully capture the dynamic switch of polymer chains and their solvation. There is a need to develop approaches that combine *in situ* spectroscopy with complementary imaging and scattering techniques to observe dynamic processes and monitor dynamic changes at the catalyst–polymer interface. For example, neutron scattering, which is sensitive to hydrogen atoms, when coupled with electrochemistry, can resolve the solvation of ligand layers and provide insights into the hydrogen bonding networks of water. *In situ* imaging techniques, e.g., electrochemical-transmission electron microscopy (EC-TEM) in a liquid cell, can capture dynamic surface changes, potentially correlated with ligand–metal coordination environment change. Coupling these *operando* measurements with multiscale computational approaches, including molecular dynamics and first-principles simulations, will be essential for quantitatively linking polymer dynamics to catalytic performance.

Data availability

No primary research results, software or code have been included, and no new data were generated or analyzed as part of this review.

Conflicts of interest

There are no conflicts to declare.



Acknowledgements

JH acknowledges continuous support from the National Science Foundation (CBET-2324346 and CHE-2102245), which has made our research in this field possible. We are also grateful for the support from the University of Connecticut through its Research Excellence Program (REP).

REFERENCES

1. L. Liu and A. Corma, *Chem. Rev.*, 2018, **118**, 4981-5079.
2. P. Prinsen and R. Luque, in *Nanoparticle Design and Characterization for Catalytic Applications in Sustainable Chemistry*, eds. R. Luque and P. Prinsen, The Royal Society of Chemistry, 2019, DOI: 10.1039/9781788016292-00001, p. 0.
3. C. Xie, Z. Niu, D. Kim, M. Li and P. Yang, *Chem. Rev.*, 2020, **120**, 1184-1249.
4. S. Cao, F. Tao, Y. Tang, Y. Li and J. Yu, *Chem. Soc. Rev.*, 2016, **45**, 4747-4765.
5. M. Muzzio, J. Li, Z. Yin, I. M. Delahunty, J. Xie and S. Sun, *Nanoscale*, 2019, **11**, 18946-18967.
6. H. Y. Younan Xia, Charles T. Campbell, *Acc. Chem. Res.*, 2013, **46**, 1671-1672.
7. H. Zhang, M. Jin, Y. Xiong, B. Lim and Y. Xia, *Acc. Chem. Res.*, 2013, **46**, 1783-1794.
8. L. Jin, S. Thanneeru, D. Cintron and J. He, *ChemCatChem*, 2020, **12**, 5932-5937.
9. L. Jin, B. Liu, S. S. Duay and J. He, *Catalysts*, 2017, **7**, 44.
10. H. Guan, C. Harris and S. Sun, *Acc. Chem. Res.*, 2023, **56**, 1591-1601.
11. L. Lu, S. Zou and B. Fang, *ACS Catal.*, 2021, **11**, 6020-6058.
12. A. H. Jenkins and J. W. Medlin, *Acc. Chem. Res.*, 2021, **54**, 4080-4090.
13. P. D. Coan, C. A. Farberow, M. B. Griffin and J. W. Medlin, *ACS Catal.*, 2021, **11**, 3730-3739.
14. Y. Kim, S. Ji and J.-M. Nam, *Acc. Chem. Res.*, 2023, **56**, 2139-2150.
15. S. Kango, S. Kalia, A. Celli, J. Njuguna, Y. Habibi and R. Kumar, *Prog. Polym. Sci.*, 2013, **38**, 1232-1261.
16. Z. B. Shifrina, V. G. Matveeva and L. M. Bronstein, *Chem. Rev.*, 2020, **120**, 1350-1396.
17. K. R. Kahsar, D. K. Schwartz and J. W. Medlin, *J. Am. Chem. Soc.*, 2014, **136**, 520-526.
18. C. A. Schoenbaum, D. K. Schwartz and J. W. Medlin, *J. Catal.*, 2013, **303**, 92-99.
19. C.-H. Lien and J. W. Medlin, *J. Catal.*, 2016, **339**, 38-46.
20. C. Majumder, *Langmuir*, 2008, **24**, 10838-10842.
21. Z. Cao, J. S. Derrick, J. Xu, R. Gao, M. Gong, E. M. Nichols, P. T. Smith, X. Liu, X. Wen and C. J. A. C. Copéret, *Angew. Chem., Int. Ed.*, 2018, **130**, 5075-5079.
22. H. Tsunoyama, N. Ichikuni, H. Sakurai and T. Tsukuda, *J. Am. Chem. Soc.*, 2009, **131**, 7086-7093.
23. P. Liu and J. K. Nørskov, *Phys. Chem. Chem. Phys.*, 2001, **3**, 3814-3818.
24. S. H. Pang, C. A. Schoenbaum, D. K. Schwartz and J. W. Medlin, *Nat. Commun.*, 2013, **4**, 2448.
25. G. Chen, C. Xu, X. Huang, J. Ye, L. Gu, G. Li, Z. Tang, B. Wu, H. Yang, Z. Zhao, Z. Zhou, G. Fu and N. Zheng, *Nat. Mater.*, 2016, **15**, 564-569.
26. S. Solomon, G.-K. Plattner, R. Knutti and P. Friedlingstein, *Proc. Natl. Acad. Sci. U.S.A.*, 2009, **106**, 1704-1709.
27. A. A. Lacis, G. A. Schmidt, D. Rind and R. A. Ruedy, *Science*, 2010, **330**, 356-359.
28. S. Akrami, Y. Murakami, M. Watanabe, T. Ishihara, M. Arita, M. Fuji and K. Edalati, *Appl. Catal., B*, 2022, **303**, 120896.
29. C. D. Koolen, W. Luo and A. Züttel, *ACS Catal.*, 2023, **13**, 948-973.
30. H. Zhao, X. Liu, C. Zeng, W. Liu and L. Tan, *J. Am. Chem. Soc.*, 2024, **146**, 23649-23662.



Open Access Article. Published on 02 Februar 2026. Downloaded on 16.02.26 11:43:13.
This article is licensed under a Creative Commons Attribution-NonCommercial 3.0 Unported Licence.

31. Z. Zhang, Y. Li, Y. Huang, H. Cheng, Y. Zhao, Z. Li, Y. Hou, L. Lei and B. Yang, *Electrochem. Commun.*, 2023, **152**, 107519.

32. Z. Sun, T. Ma, H. Tao, Q. Fan and B. Han, *Chem.*, 2017, **3**, 560-587.

33. M. G. Kibria, J. P. Edwards, C. M. Gabardo, C.-T. Dinh, A. Seifitokaldani, D. Sinton and E. H. Sargent, *Adv. Mater.*, 2019, **31**, 1807166.

34. G. Wang, J. Chen, Y. Ding, P. Cai, L. Yi, Y. Li, C. Tu, Y. Hou, Z. Wen and L. Dai, *Chem. Soc. Rev.*, 2021, **50**, 4993-5061.

35. S. X. Dou, W.-H. Lai and C. Cook, *Natl. Sci. Rev.*, 2023, **10**, nwad223.

36. Y. Wu, Z. Jiang, X. Lu, Y. Liang and H. Wang, *Nature*, 2019, **575**, 639-642.

37. S. Shen, X. Peng, L. Song, Y. Qiu, C. Li, L. Zhuo, J. He, J. Ren, X. Liu and J. Luo, *Small*, 2019, **15**, 1902229.

38. C.-T. Dinh, T. Burdyny, M. G. Kibria, A. Seifitokaldani, C. M. Gabardo, F. P. García de Arquer, A. Kiani, J. P. Edwards, P. De Luna, O. S. Bushuyev, C. Zou, R. Quintero-Bermudez, Y. Pang, D. Sinton and E. H. Sargent, *Science*, 2018, **360**, 783-787.

39. Y. Hori, K. Kikuchi and S. Suzuki, *Chem. Lett.*, 1985, **14**, 1695-1698.

40. J. Albero and H. García, in *Heterogeneous Photocatalysis: From Fundamentals to Green Applications*, eds. J. C. Colmenares and Y.-J. Xu, Springer Berlin Heidelberg, Berlin, Heidelberg, 2016, DOI: 10.1007/978-3-662-48719-8_1, pp. 1-31.

41. Z. Yin, G. T. R. Palmore and S. Sun, *Trends Chem.*, 2019, **1**, 739-750.

42. J. Huang and R. Buonsanti, *Chem. Mater.*, 2019, **31**, 13-25.

43. D. D. Zhu, J. L. Liu and S. Z. Qiao, *Adv. Mater.*, 2016, **28**, 3423-3452.

44. B. Cao, F.-Z. Li and J. Gu, *ACS Catal.*, 2022, **12**, 9735-9752.

45. W. Zhu, R. Michalsky, Ö. Metin, H. Lv, S. Guo, C. J. Wright, X. Sun, A. A. Peterson and S. Sun, *J. Am. Chem. Soc.*, 2013, **135**, 16833-16836.

46. X. Wang, J. F. de Araújo, W. Ju, A. Bagger, H. Schmies, S. Kühl, J. Rossmeisl and P. Strasser, *Nat. Nanotechnol.*, 2019, **14**, 1063-1070.

47. L. Jin, B. Liu, P. Wang, H. Yao, L. A. Achola, P. Kerns, A. Lopes, Y. Yang, J. Ho, A. Moewes, Y. Pei and J. He, *Nanoscale*, 2018, **10**, 14678-14686.

48. Y. Chen, C. W. Li and M. W. Kanan, *J. Am. Chem. Soc.*, 2012, **134**, 19969-19972.

49. S. Zhao, R. Jin and R. Jin, *ACS Energy Lett.*, 2018, **3**, 452-462.

50. J. A. Trindell, J. Clausmeyer and R. M. Crooks, *J. Am. Chem. Soc.*, 2017, **139**, 16161-16167.

51. L. Zhang, W. Wang, D. Jiang, E. Gao and S. Sun, *Nano Res.*, 2015, **8**, 821-831.

52. Z. Zhang, M. Chi, G. M. Veith, P. Zhang, D. A. Lutterman, J. Rosenthal, S. H. Overbury, S. Dai and H. Zhu, *ACS Catal.*, 2016, **6**, 6255-6264.

53. C. Cui, J. Han, X. Zhu, X. Liu, H. Wang, D. Mei and Q. Ge, *J. Catal.*, 2016, **343**, 257-265.

54. X. Zheng, P. De Luna, F. P. García de Arquer, B. Zhang, N. Becknell, M. B. Ross, Y. Li, M. N. Banis, Y. Li, M. Liu, O. Voznyy, C. T. Dinh, T. Zhuang, P. Stadler, Y. Cui, X. Du, P. Yang and E. H. Sargent, *Joule*, 2017, **1**, 794-805.

55. T. Zheng, K. Jiang and H. Wang, *Adv. Mater.*, 2018, **30**, 1802066.

56. A. Betts, V. Briega-Martos, A. Cuesta and E. Herrero, *ACS Catal.*, 2020, **10**, 8120-8130.

57. C. W. Li, J. Ciston and M. W. Kanan, *Nature*, 2014, **508**, 504-507.

58. H. Xie, T. Wang, J. Liang, Q. Li and S. Sun, *Nano Today*, 2018, **21**, 41-54.

59. X. Qin, T. Vegge and H. A. Hansen, *J. Am. Chem. Soc.*, 2023, **145**, 1897-1905.

60. J. Li, Y. Kuang, Y. Meng, X. Tian, W.-H. Hung, X. Zhang, A. Li, M. Xu, W. Zhou, C.-S. Ku, C.-Y. Chiang, G. Zhu, J. Guo, X. Sun and H. Dai, *J. Am. Chem. Soc.*, 2020, **142**, 7276-7282.

Open Access Article. Published on 02 Februar 2026. Downloaded on 16.02.26 11:43:13.
This article is licensed under a Creative Commons Attribution-NonCommercial 3.0 Unported Licence.

61. M. Khalil, G. T. M. Kadja, F. A. A. Nugroho, L. G. Sutanto, P. K. Jiwanti, F. F. Abdi, F. Hussin and M. K. Aroua, *Renew. Sustain. Energy Rev.*, 2024, **206**, 114869.

62. S. Yu, S. Louisia and P. Yang, *JACS Au*, 2022, **2**, 562-572.

63. K. Rossi and R. Buonsanti, *Acc. Chem. Res.*, 2022, **55**, 629-637.

64. H. S. Jeon, J. Timoshenko, F. Scholten, I. Sinev, A. Herzog, F. T. Haase and B. Roldan Cuenya, *J. Am. Chem. Soc.*, 2019, **141**, 19879-19887.

65. C. Kim, F. Dionigi, V. Beermann, X. Wang, T. Möller and P. Strasser, *Adv. Mater.*, 2019, **31**, 1805617.

66. Y. Kang, S. M. João, R. Lin, K. Liu, L. Zhu, J. Fu, W.-C. Cheong, S. Lee, K. Frank, B. Nickel, M. Liu, J. Lischner and E. Cortés, *Nat. Commun.*, 2024, **15**, 3923.

67. G. L. De Gregorio, T. Burdyny, A. Loiudice, P. Iyengar, W. A. Smith and R. Buonsanti, *ACS Catal.*, 2020, **10**, 4854-4862.

68. K. Manthiram, B. J. Beberwyck and A. P. Alivisatos, *J Am Chem Soc*, 2014, **136**, 13319-13325.

69. Y. Li, D. Kim, S. Louisia, C. Xie, Q. Kong, S. Yu, T. Lin, S. Aloni, S. C. Fakra and P. Yang, *Proc. Natl. Acad. Sci. U.S.A.*, 2020, **117**, 9194-9201.

70. S. Popović, M. Smiljanić, P. Jovanović, J. Vavra, R. Buonsanti and N. Hodnik, *Angew. Chem., Int. Ed.*, 2020, **59**, 14736-14746.

71. J. A. Lopez-Sanchez, N. Dimitratos, C. Hammond, G. L. Brett, L. Kesavan, S. White, P. Miedziak, R. Tiruvalam, R. L. Jenkins, A. F. Carley, D. Knight, C. J. Kiely and G. J. Hutchings, *Nat. Chem.*, 2011, **3**, 551-556.

72. Z. Niu and Y. Li, *Chem. Mater.*, 2014, **26**, 72-83.

73. D. Li, C. Wang, D. Tripkovic, S. Sun, N. M. Markovic and V. R. Stamenkovic, *ACS Catal.*, 2012, **2**, 1358-1362.

74. F. Li and Q. Tang, *J. Mater. Chem. A*, 2019, **7**, 19872-19880.

75. T. Zhang, J. He and X. Xiang, *ChemCatChem*, 2023, **15**, e202301119.

76. Q. Zhu, C. J. Murphy and L. R. Baker, *J. Am. Chem. Soc.*, 2022, **144**, 2829-2840.

77. X. Kong, J. Zhu, Z. Xu and Z. Geng, *Angew. Chem., Int. Ed.*, 2025, **64**, e202417562.

78. X. Wei, Z. Yin, K. Lyu, Z. Li, J. Gong, G. Wang, L. Xiao, J. Lu and L. Zhuang, *ACS Catal.*, 2020, **10**, 4103-4111.

79. Y. Ma, J. Wang, J. Yu, J. Zhou, X. Zhou, H. Li, Z. He, H. Long, Y. Wang, P. Lu, J. Yin, H. Sun, Z. Zhang and Z. Fan, *Matter*, 2021, **4**, 888-926.

80. J. Li, F. He, Z. Cheng, J. Chen, X. Zhang and Z. Qi, *J. Mater. Chem. A*, 2025, **13**, 12039-12056.

81. Q. Fan, G. Bao, X. Chen, Y. Meng, S. Zhang and X. Ma, *ACS Catal.*, 2022, **12**, 7517-7523.

82. M. Wan, Z. Yang, H. Morgan, J. Shi, F. Shi, M. Liu, H.-W. Wong, Z. Gu and F. Che, *J. Am. Chem. Soc.*, 2023, **145**, 26038-26051.

83. N. A. Nosratabad, Z. Jin, L. Du, M. Thakur and H. Matoussi, *Chem. Mater.*, 2021, **33**, 921-933.

84. N. Arabzadeh Nosratabad, Z. Jin, H. Arabzadeh, B. Chen, C. Huang and H. Matoussi, *Dalton Trans.*, 2024, **53**, 467-483.

85. L. Zhang, Z. Wei, S. Thanneeru, M. Meng, M. Kruzyk, G. Ung, B. Liu and J. He, *Angew. Chem., Int. Ed.*, 2019, **58**, 15834-15840.

86. Q. Luo, J. A. Adewuyi, L. Smith, F. K. Masese, Y. Chen, R. M. Kasi, A. D. Aderibigbe, S. Sun, G. Ung and J. He, *ACS Appl. Mater. Interfaces*, 2025, **17**, 43899-43908.

87. J. R. Pankhurst, Y. T. Guntern, M. Mensi and R. Buonsanti, *Chem. Sci.*, 2019, **10**, 10356-10365.

88. Z. Han, X. Wang, Z. Li, J. Gao, Z. Hu, Y. Wang, S. Li, X. Mao, Q.-h. Yang and Z. Weng, *Angew. Chem., Int. Ed.*, 2025, **64**, e202504785.

Open Access Article. Published on 02 Februar 2026. Downloaded on 16.02.26 11:43:13.
This article is licensed under a Creative Commons Attribution-NonCommercial 3.0 Unported Licence.

89. J. Chen, L. Fan, Y. Zhao, H. Yang, D. Wang, B. Hu, S. Xi and L. Wang, *Chem. Commun.*, 2024, **60**, 3178-3181.

90. K. S. Rawat, A. Mahata, I. Choudhuri and B. Pathak, *J. Phys. Chem. C*, 2016, **120**, 8821-8831.

91. S. Sung, X. Li, L. M. Wolf, J. R. Meeder, N. S. Bhuvanesh, K. A. Grice, J. A. Panetier and M. Nippe, *J. Am. Chem. Soc.*, 2019, **141**, 6569-6582.

92. J.-J. Lv, R. Yin, L. Zhou, J. Li, R. Kikas, T. Xu, Z.-J. Wang, H. Jin, X. Wang and S. Wang, *Angew. Chem., Int. Ed.*, 2022, **61**, e202207252.

93. Z. Xing, L. Hu, D. S. Ripatti, X. Hu and X. Feng, *Nat. Commun.*, 2021, **12**, 136.

94. Y. C. Tan, K. B. Lee, H. Song and J. Oh, *Joule*, 2020, **4**, 1104-1120.

95. A. Thevenon, A. Rosas-Hernández, A. M. Fontaní Herreros, T. Agapie and J. C. Peters, *ACS Catal.*, 2021, **11**, 4530-4537.

96. Y. Lin, T. Wang, L. Zhang, G. Zhang, L. Li, Q. Chang, Z. Pang, H. Gao, K. Huang, P. Zhang, Z.-J. Zhao, C. Pei and J. Gong, *Nat. Commun.*, 2023, **14**, 3575.

97. E. Shirzadi, Q. Jin, A. S. Zeraati, R. Dorakhan, T. J. Goncalves, J. Abed, B.-H. Lee, A. S. Rasouli, J. Wicks, J. Zhang, P. Ou, V. Boureau, S. Park, W. Ni, G. Lee, C. Tian, D. M. Meira, D. Sinton, S. Siahrostami and E. H. Sargent, *Nat. Commun.*, 2024, **15**, 2995.

98. M. Sun, J. Cheng and M. Yamauchi, *Nat. Commun.*, 2024, **15**, 491.

99. Z.-Z. Niu, F.-Y. Gao, X.-L. Zhang, P.-P. Yang, R. Liu, L.-P. Chi, Z.-Z. Wu, S. Qin, X. Yu and M.-R. Gao, *J. Am. Chem. Soc.*, 2021, **143**, 8011-8021.

100. M. Fang, M. Wang, Z. Wang, Z. Zhang, H. Zhou, L. Dai, Y. Zhu and L. Jiang, *J. Am. Chem. Soc.*, 2023, **145**, 11323-11332.

101. M. Fan, J. E. Huang, R. K. Miao, Y. Mao, P. Ou, F. Li, X.-Y. Li, Y. Cao, Z. Zhang, J. Zhang, Y. Yan, A. Ozden, W. Ni, Y. Wang, Y. Zhao, Z. Chen, B. Khatir, C. P. O'Brien, Y. Xu, Y. C. Xiao, G. I. N. Waterhouse, K. Golovin, Z. Wang, E. H. Sargent and D. Sinton, *Nat. Catal.*, 2023, **6**, 763-772.

102. M. D. Porter, T. B. Bright, D. L. Allara and C. E. Chidsey, *J. Am. Chem. Soc.*, 1987, **109**, 3559-3568.

103. H. Finklea, L. Robinson, A. Blackburn, B. Richter, D. Allara and T. Bright, *Langmuir*, 1986, **2**, 239-244.

104. E. Boubour and R. B. Lennox, *Langmuir*, 2000, **16**, 4222-4228.

105. R. Haag, M. A. Rampi, R. E. Holmlin and G. M. Whitesides, *J. Am. Chem. Soc.*, 1999, **121**, 7895-7906.

106. P. Fenter, A. Eberhardt and P. Eisenberger, *Science*, 1994, **266**, 1216-1218.

107. J. Aizenberg, A. J. Black and G. M. Whitesides, *Nature*, 1999, **398**, 495-498.

108. S. Chen and R. W. Murray, *Langmuir*, 1999, **15**, 682-689.

109. C. Yi, Y. Yang, B. Liu, J. He and Z. Nie, *Chem. Soc. Rev.*, 2020, **49**, 465-508.

110. L. Michalek, L. Barner and C. Barner-Kowollik, *Adv. Mater.*, 2018, **30**, 1706321.

111. Q. Luo, H. Duan, M. C. McLaughlin, K. Wei, J. Tapia, J. A. Adewuyi, S. Shuster, M. Liaqat, Steven L. Suib, G. Ung, P. Bai, S. Sun and J. He, *Chem. Sci.*, 2023, **14**, 9664-9677.

112. Y. Chae, H. Kim, D. K. Lee, U. Lee and D. H. Won, *Nano Energy*, 2024, **130**, 110134.

113. P. Chinwangso, H. J. Lee, A. C. Jamison, M. D. Marquez, C. S. Park and T. R. Lee, *Langmuir*, 2017, **33**, 1751-1762.

114. Y.-S. Shon, S. Lee, R. Colorado, S. S. Perry and T. R. Lee, *J. Am. Chem. Soc.*, 2000, **122**, 7556-7563.

115. G. M. Whitesides and P. E. J. L. Laibinis, *Langmuir*, 1990, **6**, 87-96.

116. D. Wakerley, S. Lamaison, F. Ozanam, N. Menguy, D. Mercier, P. Marcus, M. Fontecave and V. Mougel, *Nat. Mater.*, 2019, **18**, 1222-1227.

117. M. W. J. Beulen, M. I. Kastenberg, F. C. J. M. van Veggel and D. N. Reinhoudt, *Langmuir*, 1998, **14**, 7463-7467.

118. N. C. Ramos, J. W. Medlin and A. Holewinski, *ACS Appl. Mater. Interfaces*, 2023, **15**, 14470-14480.

119. H.-Q. Liang, S. Zhao, X.-M. Hu, M. Ceccato, T. Skrydstrup and K. Daasbjerg, *ACS Catal.*, 2021, **11**, 958-966.

120. J. H. Lee, S. Kattel, Z. Xie, B. M. Tackett, J. Wang, C.-J. Liu and J. G. Chen, *Adv. Funct. Mater.*, 2018, **28**, 1804762.

121. J. Pellessier, X. Gong, B. Li, J. Zhang, Y. Gang, K. Hambleton, C. Podder, Z. Gao, H. Zhou, G. Wang, H. Pan and Y. Li, *J. Mater. Chem. A*, 2023, **11**, 26252-26264.

122. L. Li, J. Chen, V. S. S. Mosali, Y. Liang, A. M. Bond, Q. Gu and J. Zhang, *Angew. Chem., Int. Ed.*, 2022, **61**, e202208534.

123. M. N. Hopkinson, C. Richter, M. Schedler and F. Glorius, *Nature*, 2014, **510**, 485-496.

124. B. Qie, Z. Wang, J. Jiang, Z. Zhang, P. H. Jacobse, J. Lu, X. Li, F. Liu, A. N. Alexandrova, S. G. Louie, M. F. Crommie and F. R. Fischer, *Science*, 2024, **384**, 895-901.

125. K. C. Edwards, M. Vasiliu, J. W. Maxwell, C. E. Castillo, D. M. Marion, R. Craciun, J. F. Hall, D. Tapu and D. A. Dixon, *J. Phys. Chem. A*, 2023, **127**, 10838-10850.

126. L. Zhang, Z. Wei, M. Meng, G. Ung and J. He, *J. Mater. Chem. A*, 2020, **8**, 15900-15908.

127. S. Thanneeru, K. M. Ayers, M. Anuganti, L. Zhang, C. V. Kumar, G. Ung and J. He, *J. Mater. Chem. C*, 2020, **8**, 2280-2288.

128. Z. Wei, M. Kayceety, A. Price, K. Wei, Q. Luo, S. Thanneeru, S. Sun and J. He, *ACS Appl. Mater. Interfaces*, 2022, **14**, 55227-55237.

129. H. Duan, Y. Lin and J. He, in *World Scientific Reference on Plasmonic Nanomaterials*, World Scientific, 2021, vol. Volume 22, pp. 409-432.

130. Y. Chen, K. Wei, H. Duan, H. Sun, Z. Yu, A. Zohaib, P. Zhu, J. He and S. Sun, *J. Am. Chem. Soc.*, 2025, **147**, 14845-14855.

131. N. Kumar, J. He and J. F. Rusling, *Chem. Soc. Rev.*, 2023, **52**, 5135-5171.

132. T. H. M. Pham, J. Zhang, M. Li, T.-H. Shen, Y. Ko, V. Tileli, W. Luo and A. Züttel, *Adv. Energy Mater.*, 2022, **12**, 2103663.

133. Y. Li, Z. Pei, D. Luan and X. W. Lou, *Angew. Chem., Int. Ed.*, 2023, **62**, e202302128.

134. S. Jia, Q. Zhu, M. Chu, S. Han, R. Feng, J. Zhai, W. Xia, M. He, H. Wu and B. Han, *Angew. Chem., Int. Ed.*, 2021, **60**, 10977-10982.

135. L. Su, Q. Hua, G. Feng, Y. Yang, H. Mei, Y. Yu, X. Chang and Z. Huang, *Adv. Funct. Mater.*, 2025, **35**, 2425636.

136. X. Fan, W. Nie, H. Tsai, N. Wang, H. Huang, Y. Cheng, R. Wen, L. Ma, F. Yan and Y. Xia, *Adv. Sci.*, 2019, **6**, 1900813.

137. M. Vosgueritchian, D. J. Lipomi and Z. Bao, *Adv. Funct. Mater.*, 2012, **22**, 421-428.

138. H. Huang, Y. Zhao, T. Cong, C. Li, N. Wen, X. Zuo, Y. Guo, H. Zhang, Z. Fan and L. Pan, *Adv. Funct. Mater.*, 2022, **32**, 2110777.

139. X. Chen, S. Jia, C. Chen, J. Jiao, J. Zhai, T. Deng, C. Xue, H. Cheng, M. Dong, W. Xia, J. Zeng, X. Xing, H. Wu, M. He and B. Han, *Adv. Mater.*, 2024, **36**, 2310273.

140. J. Cheng, L. Chen, X. Xie, K. Feng, H. Sun, Y. Qin, W. Hua, Z. Zheng, Y. He, W. Pan, W. Yang, F. Lyu, J. Zhong, Z. Deng, Y. Jiao and Y. Peng, *Angew. Chem., Int. Ed.*, 2023, **62**, e202312113.



141. G. Li, L. Huang, C. Wei, H. Shen, Y. Liu, Q. Zhang, J. Su, Y. Song, W. Guo, X. Cao, B. Z. Tang, M. Robert and R. Ye, *Angew. Chem., Int. Ed.*, 2024, **63**, e202400414.

142. C. Kim, J. C. Bui, X. Luo, J. K. Cooper, A. Kusoglu, A. Z. Weber and A. T. Bell, *Nat. Energy*, 2021, **6**, 1026-1034.

143. M. L. J. Peerlings, M. E. T. Vink-van Ittersum, J. W. de Rijk, P. E. de Jongh and P. Ngene, *ACS Catal.*, 2025, **15**, 9695-9705.

144. C. Yu, T. Lei, L. Xu, C. Jin, J. Yi, S. Liu, S. Lin, Y. Yang, H. Song, K. Wang, H. Fan, C. Zheng, X. Zhang and X. Gao, *J. Mater. Chem. A*, 2024, **12**, 17181-17192.

145. F. P. García de Arquer, C.-T. Dinh, A. Ozden, J. Wicks, C. McCallum, A. R. Kirmani, D.-H. Nam, C. Gabardo, A. Seifitokaldani, X. Wang, Y. C. Li, F. Li, J. Edwards, L. J. Richter, S. J. Thorpe, D. Sinton and E. H. Sargent, *Science*, 2020, **367**, 661-666.

146. P. Papangelakis, R. K. Miao, R. Lu, H. Liu, X. Wang, A. Ozden, S. Liu, N. Sun, C. P. O'Brien, Y. Hu, M. Shakouri, Q. Xiao, M. Li, B. Khatir, J. E. Huang, Y. Wang, Y. C. Xiao, F. Li, A. S. Zeraati, Q. Zhang, P. Liu, K. Golovin, J. Y. Howe, H. Liang, Z. Wang, J. Li, E. H. Sargent and D. Sinton, *Nat. Energy*, 2024, **9**, 1011-1020.

147. J. Sun, B. Wu, Z. Wang, H. Guo, G. Yan, H. Duan, G. Li, Y. Wang and J. Wang, *Energy Environ. Sci.*, 2025, **18**, 1027-1037.

148. J. Park, Y. Chae, C. Lee, G. Kwon, W. H. Lee, H. S. Jeon, J. Cho, D. H. Won and J. H. Koh, *ACS Catal.*, 2025, **15**, 12222-12230.

149. Y. I. Song, B. Yoon, C. Lee, D. Kim, M. H. Han, H. Han, W. H. Lee, D. H. Won, J. K. Kim, H. S. Jeon and J. H. Koh, *Adv. Sci.*, 2024, **11**, 2406281.

150. X. Ye, C. Zheng, J. Chen, Y. Gao and C. B. Murray, *Nano Lett.*, 2013, **13**, 765-771.

151. J. Mosquera, D. Wang, S. Bals and L. M. Liz-Marzán, *Acc. Chem. Res.*, 2023, **56**, 1204-1212.

152. C. J. Murphy, T. K. Sau, A. M. Gole, C. J. Orendorff, J. Gao, L. Gou, S. E. Hunyadi and T. Li, *J. Phys. Chem. B*, 2005, **109**, 13857-13870.

153. D. Muhuri, M. Sarkar, H. Duan, L. A. Hanson and J. He, *Angew. Chem., Int. Ed.*, 2025, **64**, e202516071.

154. L. Xue, Z. Gao, T. Ning, W. Li, J. Li, J. Yin, L. Xiao, G. Wang and L. Zhuang, *Angew. Chem., Int. Ed.*, 2023, **62**, e202309519.

155. X. Chen, J. Chen, N. M. Alghoraibi, D. A. Henckel, R. Zhang, U. O. Nwabara, K. E. Madsen, P. J. A. Kenis, S. C. Zimmerman and A. A. Gewirth, *Nat. Catal.*, 2021, **4**, 20-27.

156. Q. Luo, J. Tapia, L. Zhou, C.-H. Liu, M. Liaqat, H. Duan, Z. Yang, M.-P. Nieh, T. Emrick, P. Bai and J. He, *Nanoscale*, 2024, **16**, 15558-15567.

157. H.-G. Qin, Y.-F. Du, Y.-Y. Bai, F.-Z. Li, X. Yue, H. Wang, J.-Z. Peng and J. Gu, *Nat. Commun.*, 2023, **14**, 5640.

158. X.-Q. Li, G.-Y. Duan, J.-W. Chen, L.-J. Han, S.-J. Zhang and B.-H. Xu, *Appl. Catal., B*, 2021, **297**, 120471.

159. G.-Y. Duan, X.-Q. Li, G.-R. Ding, L.-J. Han, B.-H. Xu and S.-J. Zhang, *Angew. Chem., Int. Ed.*, 2022, **61**, e202110657.

160. A. H. Mamaghani, J. Liu, Z. Zhang, R. Gao, Y. Wu, H. Li, M. Feng and Z. Chen, *Adv. Energy Mater.*, 2024, **14**, 2402278.

161. M. Ding, R. W. Flaig, H.-L. Jiang and O. M. Yaghi, *Chem. Soc. Rev.*, 2019, **48**, 2783-2828.

162. C. S. Diercks, Y. Liu, K. E. Cordova and O. M. Yaghi, *Nat. Mater.*, 2018, **17**, 301-307.

163. D.-H. Nam, O. Shekhah, A. Ozden, C. McCallum, F. Li, X. Wang, Y. Lum, T. Lee, J. Li, J. Wicks, A. Johnston, D. Sinton, M. Eddaoudi and E. H. Sargent, *Adv. Mater.*, 2022, **34**, 2207088.



Open Access Article. Published on 02 Februar 2026. Downloaded on 16.02.26 11:43:13.
This article is licensed under a Creative Commons Attribution-NonCommercial 3.0 Unported Licence.

(cc) BY-NC

164. R. Freund, O. Zaremba, G. Arnauts, R. Ameloot, G. Skorupskii, M. Dincă, A. Bavykina, J. Gascon, A. Ejsmont, J. Goscianska, M. Kalmutzki, U. Lächelt, E. Ploetz, C. S. Diercks and S. Wuttke, *Angew. Chem., Int. Ed.*, 2021, **60**, 23975-24001.
165. D.-H. Yang, Y. Tao, X. Ding and B.-H. Han, *Chem. Soc. Rev.*, 2022, **51**, 761-791.
166. S. Zheng, S. Xia, Z. Ouyang, S. Bi, Y. Fu, G. Liu, Y. Wang, Q. Xu and G. Zeng, *ACS Catal.*, 2024, **14**, 18524-18534.
167. Y. Zhao, L. Zheng, D. Jiang, W. Xia, X. Xu, Y. Yamauchi, J. Ge and J. Tang, *Small*, 2021, **17**, 2006590.
168. J. Yuan, S. Chen, Y. Zhang, R. Li, J. Zhang and T. Peng, *Adv. Mater.*, 2022, **34**, 2203139.
169. M. Xu, C. Lai, X. Liu, B. Li, M. Zhang, F. Xu, S. Liu, L. Li, L. Qin, H. Yi and Y. Fu, *J. Mater. Chem. A*, 2021, **9**, 24148-24174.
170. L. Ma, W. Hu, B. Mei, H. Liu, B. Yuan, J. Zang, T. Chen, L. Zou, Z. Zou, B. Yang, Y. Yu, J. Ma, Z. Jiang, K. Wen and H. Yang, *ACS Catal.*, 2020, **10**, 4534-4542.
171. Y. Zou and S. Wang, *Adv. Sci.*, 2021, **8**, 2003579.
172. B. Peng, H. She, Z. Wei, Z. Sun, Z. Deng, Z. Sun and W. Chen, *Nat. Commun.*, 2025, **16**, 2217.
173. D.-H. Nam, O. Shekhah, G. Lee, A. Mallick, H. Jiang, F. Li, B. Chen, J. Wicks, M. Eddaoudi and E. H. Sargent, *J. Am. Chem. Soc.*, 2020, **142**, 21513-21521.
174. Y.-R. Wang, H.-M. Ding, X.-Y. Ma, M. Liu, Y.-L. Yang, Y. Chen, S.-L. Li and Y.-Q. Lan, *Angew. Chem., Int. Ed.*, 2022, **61**, e202114648.
175. C. Li, W. Ju, S. Vijay, J. Timoshenko, K. Mou, D. A. Cullen, J. Yang, X. Wang, P. Pachfule and S. J. A. C. Brückner, *Angew. Chem., Int. Ed.*, 2022, **134**, e202114707.
176. H. Zhong, M. Ghorbani-Asl, K. H. Ly, J. Zhang, J. Ge, M. Wang, Z. Liao, D. Makarov, E. Zschech, E. Brunner, I. M. Weidinger, J. Zhang, A. V. Krasheninnikov, S. Kaskel, R. Dong and X. Feng, *Nat. Commun.*, 2020, **11**, 1409.
177. S. Mukhopadhyay, R. Shimoni, I. Liberman, R. Ifraemov, I. Rozenberg and I. Hod, *Angew. Chem., Int. Ed.*, 2021, **60**, 13423-13429.
178. S. Mukhopadhyay, M. S. Naeem, G. Shiva Shanker, A. Ghatak, A. R. Kottaichamy, R. Shimoni, L. Avram, I. Liberman, R. Balilty, R. Ifraemov, I. Rozenberg, M. Shalom, N. López and I. Hod, *Nat. Commun.*, 2024, **15**, 3397.
179. Q. Yang, Q. Xu and H.-L. Jiang, *Chem. Soc. Rev.*, 2017, **46**, 4774-4808.
180. Q.-L. Zhu, J. Li and Q. Xu, *J. Am. Chem. Soc.*, 2013, **135**, 10210-10213.
181. G. Lu, S. Li, Z. Guo, O. K. Farha, B. G. Hauser, X. Qi, Y. Wang, X. Wang, S. Han, X. Liu, J. S. DuChene, H. Zhang, Q. Zhang, X. Chen, J. Ma, S. C. J. Loo, W. D. Wei, Y. Yang, J. T. Hupp and F. Huo, *Nat. Chem.*, 2012, **4**, 310-316.
182. C.-H. Kuo, Y. Tang, L.-Y. Chou, B. T. Sneed, C. N. Brodsky, Z. Zhao and C.-K. Tsung, *J. Am. Chem. Soc.*, 2012, **134**, 14345-14348.
183. M. Zhao, K. Yuan, Y. Wang, G. Li, J. Guo, L. Gu, W. Hu, H. Zhao and Z. Tang, *Nature*, 2016, **539**, 76-80.
184. T. Yan, P. Wang and W.-Y. Sun, *Small*, 2023, **19**, 2206070.
185. N. Zhang and Y. Zhang, *Chem. Eng. J.*, 2024, **499**, 156694.
186. Y. Zhang, Y. Chen, X. Wang, Y. Feng, H. Zhang and G. Zhang, *Angew. Chem., Int. Ed.*, 2023, **62**, e202302241.
187. A. Singh, S. Barman, F. A. Rahimi, A. Dey, R. Jena, R. Kumar, N. Mathew, D. Bhattacharyya and T. K. Maji, *Energy Environ. Sci.*, 2024, **17**, 2315-2325.
188. S. Chen, W.-H. Li, W. Jiang, J. Yang, J. Zhu, L. Wang, H. Ou, Z. Zhuang, M. Chen, X. Sun, D. Wang and Y. Li, *Angew. Chem., Int. Ed.*, 2022, **61**, e202114450.

Open Access Article. Published on 02 Februar 2026. Downloaded on 16.02.26 11:43:13.
This article is licensed under a Creative Commons Attribution-NonCommercial 3.0 Unported Licence.

189. C. He, D.-H. Si, L. Han, Z.-N. Xu, Z. Chen, R. Cao and Y.-B. Huang, *ACS Catal.*, 2024, **14**, 3943-3954.

190. J.-D. Yi, R. Xie, Z.-L. Xie, G.-L. Chai, T.-F. Liu, R.-P. Chen, Y.-B. Huang and R. Cao, *Angew. Chem., Int. Ed.*, 2020, **59**, 23641-23648.

191. Z.-H. Zhao, K. Zheng, N.-Y. Huang, H.-L. Zhu, J.-R. Huang, P.-Q. Liao and X.-M. Chen, *Chem. Commun.*, 2021, **57**, 12764-12767.

192. X. Min and M. W. Kanan, *J. Am. Chem. Soc.*, 2015, **137**, 4701-4708.

193. S. Lin, C. S. Diercks, Y.-B. Zhang, N. Kornienko, E. M. Nichols, Y. Zhao, A. R. Paris, D. Kim, P. Yang, O. M. Yaghi and C. J. Chang, *Science*, 2015, **349**, 1208-1213.

194. M. Lu, M. Zhang, J. Liu, Y. Chen, J.-P. Liao, M.-Y. Yang, Y.-P. Cai, S.-L. Li and Y.-Q. Lan, *Angew. Chem., Int. Ed.*, 2022, **61**, e202200003.

195. M. Zhang, M. Lu, M.-Y. Yang, J.-P. Liao, Y.-F. Liu, H.-J. Yan, J.-N. Chang, T.-Y. Yu, S.-L. Li and Y.-Q. Lan, *EScience*, 2023, **3**, 100116.

196. A. Ozden, J. Li, S. Kandambeth, X.-Y. Li, S. Liu, O. Shekhah, P. Ou, Y. Zou Finfrock, Y.-K. Wang, T. Alkayyali, F. Pelayo García de Arquer, V. S. Kale, P. M. Bhatt, A. H. Ip, M. Eddaoudi, E. H. Sargent and D. Sinton, *Nat. Energy*, 2023, **8**, 179-190.

197. T. Zhao, Q. Niu, G. Huang, Q. Chen, Y. Gao, J. Bi and L. Wu, *J. Colloid Interf. Sci.*, 2021, **602**, 23-31.

198. S. Zheng, D.-H. Si, H. Guo, Q.-J. Wu, H.-J. Zhu, Y.-B. Huang and R. Cao, *ACS Nano*, 2025, **19**, 24130-24139.

199. S. Cai, S. Tao, M. Chong, Z. Shi, X. Liu, D. Cheng and F. Chen, *ACS Appl. Mater. Interfaces*, 2024, **16**, 55267-55275.

200. Y.-M. Wang, F.-Q. Yan, Q.-Y. Wang, C.-X. Du, L.-Y. Wang, B. Li, S. Wang and S.-Q. Zang, *Nat. Commun.*, 2024, **15**, 1843.

201. C. Li, Y. Wang, C. Wang, Q. Wu, X. Lv, S. Xie, L. Kong, J. Feng, Z. Li, A.-J. Wang, J. Kang and F. Yang, *ACS Appl. Mater. Interfaces*, 2025, **17**, 26594-26603.

202. Y. Kong, B. Lyu, C. Fan, Y. Yang, X. Wang, B. Shi, J. Jiang, H. Wu and Z. Jiang, *J. Am. Chem. Soc.*, 2023, **145**, 27984-27992.

203. Z. Zhu, Y. Zhu, Z. Ren, D. Liu, F. Yue, D. Sheng, P. Shao, X. Huang, X. Feng, A.-X. Yin, J. Xie and B. Wang, *J. Am. Chem. Soc.*, 2024, **146**, 1572-1579.

204. Z. Qian, Y. Liu, Z. Lin, N. Ye, Y. Tan, F. Liu, Y. Gu, Q. Huang, H. Guo, M. Luo and S. Guo, *J. Am. Chem. Soc.*, 2025, **147**, 21877-21884.

205. M. Fang, X. Miao, Z. Huang, M. Wang, X. Feng, Z. Wang, Y. Zhu, L. Dai and L. Jiang, *J. Am. Chem. Soc.*, 2024, **146**, 27060-27069.

206. J. Yu, C. Mu, B. Yan, X. Qin, C. Shen, H. Xue and H. Pang, *Mater. Horiz.*, 2017, **4**, 557-569.

207. M. Mukoyoshi and H. Kitagawa, *Chem. Commun.*, 2022, **58**, 10757-10767.

208. L.-X. Liu, C. Qin, T. Deng, L. Sun, Z. Chen and X. Han, *J. Mater. Chem. A*, 2024, **12**, 26421-26438.

209. C. A. Trickett, A. Helal, B. A. Al-Maythalony, Z. H. Yamani, K. E. Cordova and O. M. Yaghi, *Nat. Rev. Mater.*, 2017, **2**, 17045.

210. Q. Wang and D. Astruc, *Chem. Rev.*, 2020, **120**, 1438-1511.

211. Y. Zhang, X.-Y. Zhang and W.-Y. Sun, *ACS Catal.*, 2023, **13**, 1545-1553.

212. D.-H. Nam, O. S. Bushuyev, J. Li, P. De Luna, A. Seifitokaldani, C.-T. Dinh, F. P. García de Arquer, Y. Wang, Z. Liang, A. H. Proppe, C. S. Tan, P. Todorović, O. Shekhah, C. M. Gabardo, J. W. Jo, J. Choi, M.-J. Choi, S.-W. Baek, J. Kim, D. Sinton, S. O. Kelley, M. Eddaoudi and E. H. Sargent, *J. Am. Chem. Soc.*, 2018, **140**, 11378-11386.

213. X. Xie, X. Zhang, M. Xie, L. Xiong, H. Sun, Y. Lu, Q. Mu, M. H. Rummeli, J. Xu, S. Li, J. Zhong, Z. Deng, B. Ma, T. Cheng, W. A. Goddard and Y. Peng, *Nat. Commun.*, 2022, **13**, 63.

214. Y. Hori, H. Wakebe, T. Tsukamoto and O. Koga, *Surf. Sci.*, 1995, **335**, 258-263.

215. S. Mezzavilla, S. Horch, I. E. L. Stephens, B. Seger and I. Chorkendorff, *Angew. Chem., Int. Ed.*, 2019, **58**, 3774-3778.

216. A. Kim, C. Kim, T. Waltmann, T. Vo, E. M. Kim, J. Kim, Y.-T. Shao, A. Michelson, J. R. Crockett, F. C. Kalutantirige, E. Yang, L. Yao, C.-Y. Hwang, Y. Zhang, Y.-S. Liu, H. An, Z. Gao, J. Kim, S. Mandal, D. A. Muller, K. A. Fichthorn, S. C. Glotzer and Q. Chen, *Nature*, 2025, **646**, 592-600.

217. N. L. Dominique, A. Chandran, I. M. Jensen, D. M. Jenkins and J. P. Camden, *Chem. Eur. J.*, 2024, **30**, e202303681.

218. D. Kim, S. Yu, F. Zheng, I. Roh, Y. Li, S. Louisia, Z. Qi, G. A. Somorjai, H. Frei, L.-W. Wang and P. Yang, *Nat. Energy*, 2020, **5**, 1032-1042.

219. H. Dridi, C. Comminges, C. Morais, J.-C. Meledje, K. B. Kokoh, C. Costentin and J.-M. Savéant, *J. Am. Chem. Soc.*, 2017, **139**, 13922-13928.

220. C. Costentin, J. C. Canales, B. Haddou and J.-M. Savéant, *J. Am. Chem. Soc.*, 2013, **135**, 17671-17674.

221. W. Xie, J. Xu, U. Md Idros, J. Katsuhira, M. Fuki, M. Hayashi, M. Yamanaka, Y. Kobori and R. Matsubara, *Nat. Chem.*, 2023, **15**, 794-802.

222. S. Thanneeru, J. K. Nganga, A. S. Amin, B. Liu, L. Jin, A. M. Angeles-Boza and J. He, *ChemCatChem*, 2017, **9**, 1157-1162.

223. W. W. Kramer and C. C. L. McCrory, *Chem. Sci.*, 2016, **7**, 2506-2515.

224. J. M. Vadillo, L. Gómez-Coma, A. Garea and A. Irabien, *Membranes*, 2020, **10**, 234.

